TAMPEREEN TEKNILLINEN YLIOPISTO
TAMPERE UNIVERSITY OF TECHNOLOGY

MWANGI STANLEY NJENGA

BANDLIMITED DIGITAL PREDISTORTION OF WIDEBAND RF POWER AMPLIFIERS

Master of Science Thesis

Examiner: Prof. Mikko Valkama
Examiner and topic approved by the
Faculty Council of the Faculty of
Computing and Electrical Engineering
on 31st May 2017

ABSTRACT

MWANGI STANLEY NJENGA: BandLimited Digital Predistortion of Wideband RF Power Amplifiers
Tampere University of Technology
Master of Science Thesis, 68 pages, 2 Appendix pages
Master's Degree Programme in Electrical Engineering
Major: Wireless Communications
Examiner: Prof. Mikko Valkama
Keywords: Adaptive filters, behavioral modeling, carrier aggregation, digital predistortion, LTE/LTE-A, nonlinear distortion, power amplifiers.

The increase in the demand for high data rates has led to the deployment of wider bandwidths and complex waveforms in wireless communication systems. Multicarrier waveforms such as orthogonal frequency division multiplexing (OFDM) employed in modern systems are very sensitive to the transmitter chain nonidealities due to their high peak-to-average-power-ratio (PAPR) characteristic. They are therefore affected by nonlinear transmitter components particularly the power amplifier (PA). Moreover, to enhance power efficiency, PAs typically operate near saturation region and hence become more nonlinear. Power efficiency is highly desirable especially in battery powered and portable devices as well as in base stations. Hence there is a clear need for efficient linearization algorthms which improve power efficiency while maintaining high spectral efficiency.

Digital predistortion (DPD) has been recognized as one of the most effective methods in mitigating PA nonlinear distortions. The method involves the application of inverse PA nonlinear function upstream of the PA such that the overall system output has a linear amplification. The computation of the nonlinearity profile and the inversion of the PA function are particularly difficult and complicated especially when involving wideband radio access waveforms, and therefore memory effects, which are being employed in modern communication systems, such as in Long Term Evolution/Advanced (LTE/LTE-A). In the recent technical literature, different approaches which focus on the linearization of specific frequency bands or sub-bands only have been developed to alleviate this problem, thereby reducing the complexity of DPD.

In this thesis, we focus on the development and characterization of a bandlimited

DPD solution specifically tailored towards the linearization at and around the main carrier(s) in single carrier deployment or contiguous carrier aggregation of two or more component carriers. In terms of parameter identification, the solution is based on the reduced-complexity closed-loop decorrelation-based parameter learning principle, which is also able to track time-varying changes in the transmitter components adaptively. The proposed bandlimited solution is designed to linearize the inband and out-of-band (OOB) distortions in the immediate vicinity of the main carrier(s) while assuming the distortions more far away in the spectrum are suppressed by transmit or duplex filters. This is implemented using FIR filters to limit the bandwidth expansion during basis functions generation and to restrain the bandwidth of the feedback observation signal, thus reducing the DPD sample rates in both the main path processing and the parameter learning. The performance of the proposed bandlimited DPD solution is evaluated using comprehensive simulations involving memoryless and memory-based PA models, as well as true RF measurements using commercial LTE-A base station and mobile device PAs. The achieved results validate and demonstrate efficient suppression of inband and OOB distortions in real-world application scenarios. Furthermore, the bandlimited DPD consistently outperforms the conventional DPD solutions in the memory-based PA model and practical PA scenarios in suppressing the OOB distortion in the immediate vicinity of the main carrier(s) by approximately 1 - 2 dB. The results provide sufficient grounds for the application of the bandlimited DPD solution in the classical single carrier deployment or in contiguous carrier aggregation of two or more component carriers where conventional DPD solutions would otherwise be highly complex.

PREFACE

This thesis work was carried out at the Department of Electronics and Communication Engineering, Tampere University of Technology, Finland. First of all, I would like to thank Prof. Mikko Valkama for accepting me to join his research group and guiding me through the research work. I am also very grateful to MSc. Mahmoud Abdelaziz and Dsc. Adnan Kiayani for the advice, guidance, support, and patience they gave me in the entire period of the work. Special thanks to my colleagues Zeeshan Waheed and Weijie Zhu for their company and assistance during the thesis period and course work.

My study in Finland was generously supported by my parents, Mr. Sammy Mbugua and Mrs. Ann Mwangi, and I will always be indebted for their love and care during my education. I am also glad to my brothers for the unwaning encouragement and support. This thesis work was also supported by Nokia Bells Labs and Tekes through the 5G-TRX research project.

Special thanks go to all my friends I met in Tampere and overall in Finland; Ferdinand Muriyesu, Alain Itangishaka, Eunice Kamau, Simon Kamau, Joseph Gichuru, and Edward Amayo, among others.

I will forever be grateful to Finland and Tampere University of Technology for offering me an opportunity to study and enjoy tuition-free yet high-quality education.

Tampere, 6.9.2017

Stanley Mwangi

TABLE OF CONTENTS

LIST OF FIGURES

LIST OF TABLES

LIST OF ABBREVIATIONS

ACLR	Adjacent Channel Leakage Ratio
ADC	Analog-to-Digital Converter
AM/AM	Amplitude-to-Amplitude
AM/PM	Amplitude-to-Phase
BS	Base Station
CA	Carrier Aggregation
CC	Component Carrier
DAC	Digital-to-Analog Converter
DPD	Digital Predistortion
DSP	Digital Signal Processing
EVM	Error Vector Magnitude
FDD	Frequency Division Duplex
FIR	Finite Impulse Response
FLOPS	Floating Point Operations per Second
GMP	Generalized Memory Polynomial
ILA	Indirect Learning Architecture
IMD	Inter Modulation Distortion
LPF	Low Pass Filter
LS	Least Squares
LTE-A	Long Term Evolution - Advanced
OFDM	Orthogonal Frequency Division Multiplexing
PA	Power Amplifier
PAPR	Peak to Average Power Ratio
PH	Parallel Hammerstein
PSD	Power Spectral Density
SNL	Static Non-Linear
UE	User Equipment

1. INTRODUCTION

1.1 Background and Motivation

The evolution of the internet technologies has led to the demand for higher data rates in mobile communication networks due to the ever-increasing number of users and online services. By contrast, spectrum scarcity is a true challenge in achieving expected data rates, while maintaining low-cost and reliable transmitter architectures. Advances in signal processing and wireless communication methods have steadily improved the cellular communication standards since the advent of digital mobile communication in the late 1980s and early 1990s. The development and subsequent adoption of multicarrier modulation (MCM) schemes, such as orthogonal frequency division multiplexing (OFDM), have offered significant improvements in the performance of wireless systems under challenging channel conditions. The bandwidth of the radio channels has consequently expanded from 200 kHz in Global System of Mobile (GSM) to a theoretical maximum of 100 MHz in contiguous carrier aggregation (CA) of component carriers (CCs) case of long term evolution advanced (LTE-A) [1].

Wireless communication systems involve signal transmission and reception which entails both analog and digital signal processing (DSP). In the transmission chain, a digital baseband signal is generated and converted to analog form for radio propagation. This consists of three crucial operations namely: digital signal generation, digital-to-analog (DAC) conversion, and RF front-end processing [2]. Figure 1.1 shows a conceptual block diagram of a digital transmission system illustrating the signal processing stages before radio propagation. The power amplification is the last processing stage the signal undergoes before transmission. While DSP at the signal generation offers high data rates, flexibility, and spectral efficiency, the impairments in the analog RF front-end can cause substantial signal degradation, and thus constitute one major challenge [3]. In LTE-A systems, the effects of RF Impairments become more challenging due to the high peak-to-average-power-ratio (PAPR) pro-

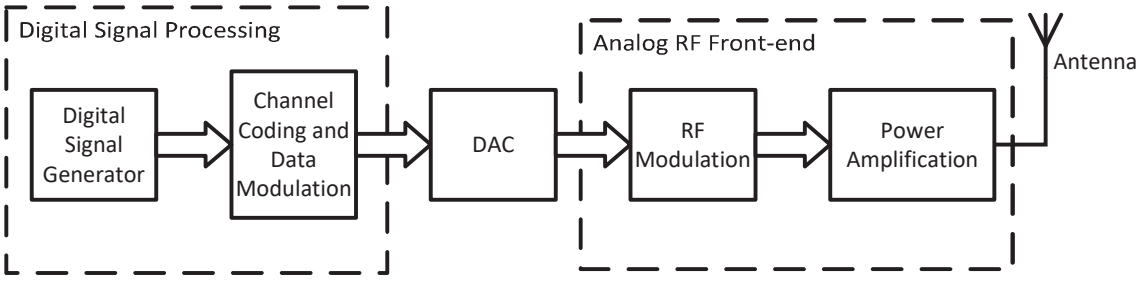

Figure 1.1 *A High level block diagram of a wireless transmission system.*

file of OFDM waveforms [4], which further increase the signal degradation. The RF impairments are caused by, among others, the power amplifier (PA) that is employed in the RF front-end to achieve the needed transmission power levels. PAs are inherently nonlinear [5], and introduce unwanted emissions when operated near the saturation region, interfering with adjacent frequency bands and the main channel band. The emissions emanate from harmonic and intermodulation distortions (IMD) which are integer multiples and linear combinations of the input frequencies, respectively. The unwanted emission limits in wireless systems are defined in the 3GPP standard on LTE/LTE-A and are strictly regulated by the International telecommunication union radio communication sector (ITU-R) and other regulatory bodies [1, 6]. Furthermore, in frequency division duplex (FDD), the IMD and harmonic components may fall in the own receiver band, thus possibly desensitizing it [7, 8].

The straight forward and simple method of reducing the spectral emissions is applying back-off to the input signal [1]. However, this compromises the power amplifier efficiency and reduces the coverage distance and throughput of the transmitter. These are highly undesirable consequences given the need to reduce the operational cost of base stations, and increase the battery life of mobile user equipment (UE). Therefore, better linearization solutions are necessitated by these unfavorable effects. Linear filtering methods are easily employed in the transmitter to remove unwanted emissions that are far from the channel spectrum. A problematic situation arises in the case of inband distortion and spectral regrowth, where nonlinear components fall in the immediate vicinity of the assigned channel bands. Linear filters cannot be used to alleviate inband distortions, while very high order filters would be required to effectively reduce the spectral regrowth below the emission limits, thereby increasing the computational complexity and cost of the transmitter design.

In [9] and [10], better linearization solutions have been proposed and extensively studied. Digital predistortion (DPD) has been identified and adopted as the defacto linearization method due to its accuracy, low-complexity, and cost-effectiveness as well as high linearity near the saturation region[11, 12, 13]. DPD involves the inversion of the PA input/output relationship/transfer function and applying it before the PA such that the overall output of the cascaded system has a linear gain. The success of a predistorter is dependent on the accuracy of behavioral modeling of the PA in terms of representing the nonlinearities under wide range of conditions, and the estimation of the inverse function of the DPD. Among the conditions that are considered during modeling include complexity, stability, memory effects, time-invariance, and causality. However, due to amplifier aging and other inevitable changes, the behavioral model may changes over time. Hence, fixed DPD solutions may not be applicable in modern radio systems which employ waveforms that have high PAPR profiles [9], where a slight change in phase or gain may violate emission specifications by 3GPP.

Adaptive DPD is developed to track RF circuitry aging process, environmental conditions, as well as stimulus changes, and consequently adjust the parameters, especially in high power and linearity applications [9, 10]. The inverse of the PA transfer function is computed adaptively by observing the output and applying it to the predistorter to maintain linear amplification. Different variants of adaptive DPD have been developed in the literature. Conventional DPD, also known as full-band DPD, aims at suppressing all the unwanted emissions in the entire transmission band, while subband DPD methods are tailored to linearize predetermined frequencies [14]. In [15], a flexible full-band DPD is proposed and it provides improved linearization at a targeted range of frequency bands, by optimizing DPD coefficients. Subband DPD is particularly attractive in battery powered devices where computational complexity may prohibit the deployment of full-band DPD in carrier aggregation with wide carrier spacing [16].

In [17, 18, 19], different behavioral models have been presented and their corresponding accuracy and complexity analyzed. The volterra series has demonstrated best performance in representing PA nonlinearities [18]. To reduce its complexity, truncated versions of the model have been developed by relaxing some of the above conditions. They include, among others, the generalized memory polynomial (GMP), parallel hammerstein (PH), and dynamic deviation reduction-based Volterra series (DDR) models. For instance, the GMP model is shown to have the

highest accuracy vs. floating point operations per second (FLOPS) followed by the PH model, hence a low computational cost [17].

Volterra series and its truncated versions are, in general, based on polynomial functions to represent PA nonlinearity orders. Thus, higher order representations of the PA nonlinearities result in an increase in the bandwidth required for feedback observation receiver and basis functions generation. This is particularly prohibitive when the transmit signal bandwidth is extremely wide, e.g. in the case of LTE-A where five, 20 MHz component carriers (CCs) are concatenated for 100 MHz bandwidth in contiguous carrier aggregation (CA) transmission scenario [1]. The required bandwidth for feedback observation would be 500 MHz (for fifth order nonlinearity), which would require very high speed ADCs and highly wideband transceivers, complicating the DPD system design. In most instances, the nonlinearity suppression performance may be relaxed when the bandwidth is very wide, and only a certain portion of distortion in the immediate vicinity of the input channel needs to be linearized, e.g. two or three times the channel bandwidth. Besides, a bandpass filter may be used at the PA output or a cavity filter at the duplexer of a FDD transceiver, to filter out the spectral regrowth beyond the band, as illustrated in figure 1.2.

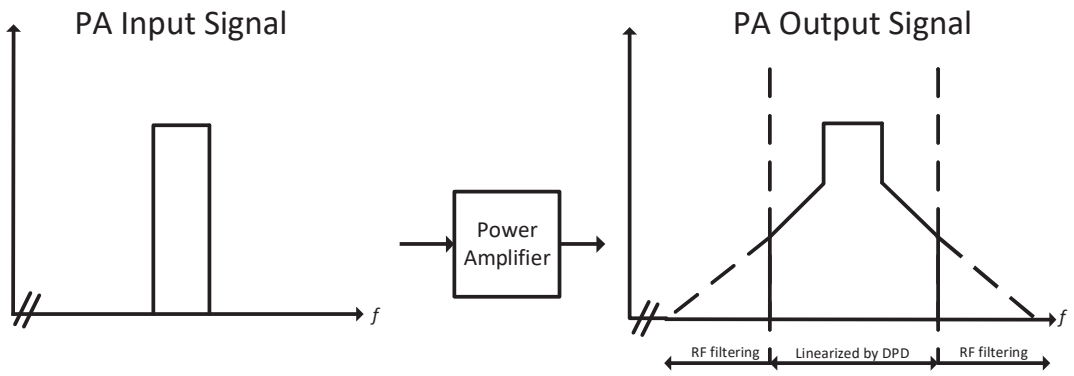

Figure 1.2 *An illustration Diagram of Band-limited DPD. The DPD linearization is performed in the immediate vicinity of the carrier signal, and the rest of the nonlinearity is suppressed by an RF transmit filter.*

In [20], a general volterra model is modified into a bandlimited Volterra-based series by using a filtering function in time domain to transform the volterra operators into bandlimited functions before been multiplied by their respective coefficients, yielding a bandlimited output. The algorithm is then employed on a conventional DPD system in [21] to produce a bandlimited version, whose flexibility, performance,

and practicality are enhanced, from the bandwidth constraint point of view.

1.2 Scope and Outline of the Thesis

In this thesis, a low-complexity bandlimited DPD concept is introduced for the linearization of wideband single carrier or contiguous CA transmission scenarios. The proposed bandlimited DPD solution is based on designing a predistorter before the PA which injects the unwanted emissions within and in the immediate vicinity of the Tx band into the PA input, with opposite phase, such that the PA output signal is free from unwanted emissions introduced by the PA in the linearized band. This is achieved by applying the bandlimited concept proposed in [21] and adopting the closed-loop decorrelation-based learning principle for parameter learning, instead of the indirect learning architecture (ILA). The bandlimiting is done to control the bandwidth expansion of the DPD parameters prior to the learning process. This is achieved by employing a low pass filter (LPF) to filter out the unwanted frequencies of the baseband equivalent signals.

The decorrelation-based learning aims at minimizing the correlation between the nonlinear basis functions generated from the input signal and the feedback nonlinear distortion signal computed from output signal observed by a feedback receiver, such that the nonlinear distortion at the PA output is reduced. The decorrelation-based principle has been demonstrated to offer similar or even better linearization performance compared to ILA-based learning methods in suppressing the unwanted emissions at and around main carrier(s) as well as in the spurious region [22, 23].

Static nonlinear (SNL) basis functions are generated from the input signal using the PH model in [19]. These are then filtered and decimated by a LPF whose bandwidth is less than the maximum nonlinearity order of the PA, and used for DPD parameter learning. Similar LPF is also used to filter and decimate the feedback observation signal. This results in the reduction of the sample rates and the bandwidth required for the entire DPD, both in the basis functions generation and DPD parameter learning. The proposed bandlimited DPD solution linearization performance is evaluated in comparison with the conventional DPD solutions using the well known metrics, namely the error vector magnitude (EVM) and the adjacent channel leakage ratio (ACLR).

The rest of the thesis is organized as follows. Chapter 2 of the thesis reviews the most

popular PA behavioral models, both memory-less and memory based. In Chapter 3, an overview of methods used in the mitigation of power amplifier nonlinear distortion is presented whereas in Chapter 4, a comprehensive mathematical and theoretical framework of the bandlimited DPD concept and system is presented. Simulation and RF measurement results of the developed DPD solution are presented in Chapter 5. Finally, Chapter 6 concludes the thesis.

2. POWER AMPLIFIER BEHAVIORAL MODELING

Behavioral modeling, also known as black-box modeling approach, builds on the rigorous acquisition of the input and output signal observations of the PA. The PA is considered a black box with only input and output signals been measured under appropriate PA excitation. Mathematical relations are then formulated to suitably describe all signal interactions between the input and output signal relations [24]. As such, there is a simplification of the entire process of characterizing the PA, as only limited prior information of the PA is required while ignoring the details of the RF circuitry.

Behavioral modeling, therefore, provides the necessary PA information which is required for a complete system level simulation, before the actual measurement setup is implemented. Behavioral models are broadly classified as neural networks (NNs) or Volterra models [19]. The Volterra type of models are in the form of a Taylor series with selected amount of nonlinear order terms with memory. Furthermore, the Volterra series may have many parameters and become very large or converge slowly, hence becoming extremely difficult to identify and formulate the behavioral model. In some cases, the PA is not driven deep into saturation, and hence only moderate nonlinearity terms and memory effect are present in the PA output [25]. Moreover, in [17], the pruned Volterra series models have been shown to accurately represent the PA nonlinear behavior at considerably low identification complexity. Hence, simplified versions of the Volterra series have been developed. In this chapter, we discuss the widely used memoryless and memory-based PA behavioral models.

2.1 Memoryless Nonlinear Models

In this section, the modeling and mathematical representation of the memoryless models are presented. Memoryless nonlinear models map the PA input to the output

when only considering the bandpass nonlinearities. Essentially, we are interested in the bandpass region where RF transmission occurs. All the output nonlinearities are associated with the instantaneous input only, and not dependent on past inputs. The mapping between the input and output signals is expressed as [26]

$$y_{rf}(n) = F[x_{rf}(n)] \tag{2.1}$$

where $x_{rf}(n)$ and $y_{rf}(n)$ are the bandpass input and output signals, respectively, at time n, while $F(.)$ is the function of the nonlinearity. The function is, however, insufficient due to the nature of the bandpass signal whose phase and amplitude vary in every period. Complex envelope signals, with constant phase and amplitudes are therefore used and read

$$x_{rf}(n) = A.\cos(\omega_c n + \Theta) \tag{2.2}$$

where A is the amplitude and Θ is the phase. This yields a periodic signal that can be described using the Fourier series and can be simplified to

$$y_{rf}(n) = F[A.\cos(\alpha)] \tag{2.3}$$

where $\alpha = \omega_c t + \Theta$. Using the Fourier Series, the output is represented by

$$y(\alpha) = a_0 + \sum_{k=1}^{\infty}(a_k \cos(k\alpha) + b_k \sin(k\alpha)) \tag{2.4}$$

where

$$a_k = \frac{1}{\pi}\int_0^{2\pi} F[A.\cos(\alpha)]\cos(k\alpha)d\alpha \tag{2.5}$$

and

$$b_k = \frac{1}{\pi}\int_0^{2\pi} F[A.\cos(\alpha)]\sin(k\alpha)d\alpha. \tag{2.6}$$

a_0 in equation (2.4) is the DC term, and k is the harmonic index. The rest of the terms are the harmonic components at the angular frequency, ω_c. In bandpass, A and α vary slowly compared to the carrier period, and its harmonics will become frequency bands around the harmonics of the carrier signal. Since we are interested in the signal around the carrier frequency, the output can be approximated as

$$y_{rf}(n) \cong a_1 \cos(w_c n + \Theta) + b_1 \sin(w_c n + \Theta) \tag{2.7}$$

where a_1 and b_1 are functions of A, Θ, and F. Incorporating A, Θ, and F in the equation, it can be rewritten as

$$y_{rf}(n) = f_A(A(n))\cos(\omega_c n + \Theta(n) + f_\Theta(A(n))). \tag{2.8}$$

Equations (2.1) and (2.8) in baseband exponential form are written as

$$x(n) = A(n)e^{j\Theta(n)} \tag{2.9}$$

and

$$y(n) = f_A(A(n))e^{j(\Theta(n)+f_\Theta(A(n)))} \tag{2.10}$$

respectively. From equation(2.10), $f_A(.)$ maps the input signal amplitude to the amplitude of the output, while $f_\Theta(.)$ maps the baseband input amplitude to the phase of the output in the baseband representation. $f_A(.)$ and $f_\Theta(.)$ are referred to as amplitude-to-amplitude (AM/AM) and amplitude-to-phase (AM/PM) mapping/conversions respectively. The AM/AM and AM/PM distortions are important criteria in quantifying the performance of a PA based on the diversion from linear gain curve and phase shift, respectively [10].

Based on the AM/AM and AM/PM conversions, the PA memoryless nonlinear models can be broadly categorized into two classes namely, strictly or quasi-memoryless models. Strictly memoryless models arise when the AM/PM is a constant, and in this case, it does not vary with $A(n)$ (usually in baseband transmission). Quasi-memoryless nonlinear amplifier models are obtained when the transmission is done in passband region, and hence both AM/AM and AM/PM conversions are not constant due to the introduction of both amplitude and phase distortions to the output signal. The power amplifier has short-term memory in this case since the signal time interval in memory is short compared to the period of signal envelope [27]. However, in baseband, PAs still exhibits memoryless input/output relationship.

2.1.1 Memoryless Polynomial Model

The model uses polynomial functions to fit the AM/AM and AM/PM mappings. In baseband representation, the PA is given by [28]

$$y(n) = \sum_{p=0}^{P} c_{2p+1}|x(n)|^{2p}x(n) \tag{2.11}$$

where $y(n)$ is the output signal, $x(n)$ is the input signal in equation(2.9) , and c_{2p+1} is the baseband coefficient of $(2p+1)$ nonlinear term. Only the odd-order nonlinearity coefficients are in the baseband representation as even order terms lie far from the passband and are easily filtered out. The AM/AM and AM/PM mappings are obtained from equation (2.11) and read

$$f_A(A) = \Big| \sum_{p=0}^{P} c_{2p+1} |A(n)|^{2p+1} \Big| \tag{2.12}$$

$$f_\Theta(A) = \angle \Big(\sum_{p=0}^{P} c_{2p+1} |A(t)|^{2p+1} \Big). \tag{2.13}$$

When the nonlinearity coefficients are real valued (in strictly memoryless case), the AM/PM conversion is zero, while complex valued coefficients yield non-zero AM/PM indicating quasi-memoryless nonlinearity.

The memoryless nonlinear model has been applied in predistorters for the development of nonlinear estimators and identification of wiener systems in [29] and [30], respectively.

2.1.2 Saleh Model

The model was proposed by A.A.M. Saleh in 1981 in [31] and was initially targeted for modeling travelling-wave tube (TWT) amplifiers. The AM/AM and AM/PM mapping functions are,

$$f_A(A) = \frac{\alpha_a A(n)}{1 + \beta_a (A(n))^2} \tag{2.14}$$

$$f_\Theta(A) = \frac{\alpha_\Theta (A(n))^2}{1 + \beta_\Theta (A(n))^2} \tag{2.15}$$

respectively, where α_a, α_Θ, β_a, and β_Θ are the four characteristic parameters of AM/AM and AM/PM mappings. The model was further extended in the modeling of power amplifiers in general for both memoryless (frequency independent) and memory-based (frequency dependent) applications. Among its application are in characterization of PA nonlinearities in transmission systems [32], and design of adaptive predistorters for high power PAs [33].

2.1.3 Ghorbani Model

The model was proposed in [34] as an advancement of the Saleh model to make it applicable for modeling solid state power amplifier (SSPA). Unlike the TWT amplifiers, the SSPAs don't have very large roll offs at saturation and the AM/PM mapping is much smaller. The AM/AM and AM/PM conversions are written as

$$f_A(A) = \frac{\alpha_0(A(n))^{\alpha_1}}{1+\alpha_2(A(n))^{\alpha_1}} + \alpha_3 A(n) \tag{2.16}$$

$$f_\Theta(A) = \frac{\beta_0(A(n))^{\beta_1}}{1+\beta_2(A(n))^{\beta_1}} + \beta_3 A(n) \tag{2.17}$$

where α_0,α_0, α_0, α_0, β_0, β_1, β_2, and β_3 are the model parameters in [34]. The AM/AM mapping curve for small-signal amplification is in exponential form, while the AM/PM conversion has a logarithmic shape instead of linear curves as in the Saleh Model.

2.1.4 Rapp Model

The Rapp model takes a different approach in behavioral modeling by totally neglecting the AM/PM mapping [35]. It assumes the phase distortions are negligible, and hence in consequence in characterizing a PA. The AM/AM relationship is given by

$$f_A(A) = \frac{\kappa A(n)}{\left(1+\left(\frac{\kappa A(n)}{A_0(n)}\right)^{2p}\right)^{1/2p}} \tag{2.18}$$

where κ is the signal gain, $A_0(t)$ is the saturation amplitude at the output, p is the smoothness parameter of the transition from linear to saturated state. The model assumes a linear performance for small-signal input, whereas at high signal levels, the output begins to saturate approaching a constant value.

2.1.5 White Model

The model was proposed in [36] to accurately model SSPAs nonlinearities in the ka-band (26GHz - 40GHz). It outperforms the Rapp, Ghorbani, and Saleh models in nonlinearity modeling at high frequency bands. The AM/AM and AM/PM

conversions are given by

$$f_A(A) = a_0(1 - e^{-a_1 A}) + a_2 A e^{-a_3 A^2} \tag{2.19}$$

$$f_\Theta(A) = \begin{cases} b_0(1 - e^{-b_1(A-b_2)}), & A \geq b_2 \\ 0, & A < b_2 \end{cases} \tag{2.20}$$

where a_0 and a_1 are the parameters representing the amplitude saturation level and linear region gain, respectively, while a_2 and a_3 are used for matching the nonlinearity in the AM/AM conversion. The parameters b_0, b_1, and b_2 are used to control the magnification, the steepness, and the shift alongside the input amplitude axis, respectively.

2.2 Memory-Based Nonlinear Models

In the previous section, we discussed PA models that deal with frequency independent cases, where the input signal bandwidth is much less than bandwidth of the amplifier, and hence the frequency response of the PA is flat. However, when wideband input signals are used for radio transmission, the PA exhibits frequency dependent behaviour and therefore a frequency selective response[18, 19, 24]. Besides, the PA nonlinearity cannot be purely defined by instantaneous mapping between the input and output signals. In the real operating environment, the PA output is also dependent on the previous input values due to delay caused by thermal and electrical effects in the PA circuitry [37].

For accurate system-level simulations, the inclusion of the PA memory (dependence on past inputs) in behavioral models becomes imperative to establish a comprehensive mapping between the PA input and output signals. Long term memory is used to refer to the delay caused by thermal and memory effects. In the quasi-memoryless case, the short-term memory was used to describe the phase distortion introduced by the use of complex-valued signals in passband transmission.

In this section, we will present the common models applied in literature to characterize the amplifier nonlinearity. We start with the Volterra series and its truncated versions and finalize with the memory-based Saleh model.

2.2.1 Volterra Series

The Volterra series presents the most extensive model for representing nonlinear systems with memory, with the least amount of error. In the discrete time domain, it can be written as [38]

$$\begin{aligned} y_{rf}(n) = {} & w_0 \\ & + \sum_{\tau_1=0}^{\infty} w_1(\tau) x_{rf}(n-\tau_1) \\ & + \sum_{\tau_1=0}^{\infty}\sum_{\tau_2=0}^{\infty} w_2(\tau_1,\tau_2) x_{rf}(n-\tau_1) x_{rf}(n-\tau_2) \\ & + ... \\ & + \sum_{\tau_1=0}^{\infty}\sum_{\tau_2=0}^{\infty} ... \sum_{\tau_p=0}^{\infty} w_p(\tau_1,\tau_2,...\tau_p) x_{rf}(n-\tau_1) x_{rf}(n-\tau_2) ... x_{rf}(n-\tau_p) \end{aligned} \tag{2.21}$$

where $y_{rf}(n)$ and $x_{rf}(n)$ are the input and output signals in the passband region, respectively. The functions w_0 $w_1(\tau)$, $w_2(\tau_1,\tau_2)$, and $w_p(\tau_1,\tau_2,...\tau_p)$ are the Volterra kernels (the model parameters). They represent the nonlinearity orders of the system. For instance, w_0 is the zeroth-order kernel (the DC term), and w_1 is the 1st order kernel (linear filter), and the rest are higher order convolutions. The block diagram in Figure 2.1 illustrates the Volterra series. The series is written more

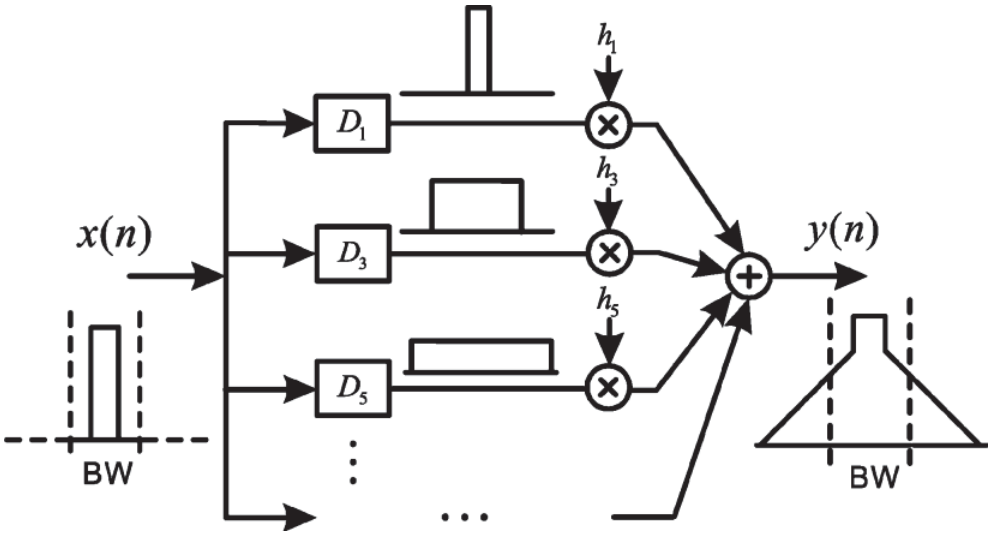

Figure 2.1 *A simple block diagram illustrating the Volterra model in [20].*

compactly and simplified as [39]

$$y_{rf}(n) = \sum_{p=1}^{\infty} \sum_{\tau_1=0}^{\infty} \cdots \sum_{\tau_p=0}^{\infty} h_p(\tau_1, \cdots, \tau_p) D_p(x_{rf}(n)) \tag{2.22}$$

where $h_p(\tau_1, \cdots, \tau_p)$ are the Volterra model parameters, and

$$D_p(x_{rf}(n)) = \prod_{p=1}^{P} x_{rf}(n - \tau_p) \tag{2.23}$$

where $D_p(.)$ is the pth-order Volterra operator. The Volterra series in the above equations is very complicated, especially when a large number of parameters are required to represent high degree of nonlinearity and memory depth. This increases the complexity in the identification of parameters and number of convolutions during system level simulation. Therefore, it becomes very complex to use it in the above forms. To mitigate the model complexity and improve its performance, several approaches have been devised, which include pruning and dynamic reduction techniques.

The dynamic deviation reduction (DDR)-based Volterra series was proposed in [40], and involves the separation and control of Volterra coefficients from different dynamic orders. The model is shown to reduce complexity without compromising the system performance, by using a very small number of parameter to represent both nonlinearity and memory depth. The model's number of parameters increase almost linearly with the nonlinearity order and memory depth, unlike in classical Volterra series where the number of coefficients increase exponentially.

The DDR-based Volterra series is written as

$$\begin{aligned} y_{rf}(n) = & \sum_{p=1}^{P} h_{p,0}(0, \ldots, 0) x_{rf}^{p}(n) \\ & + \sum_{p=1}^{P} \left\{ \sum_{r=1}^{p} \left[x_{rf}^{p-r}(n) \sum_{\tau_1=1}^{M} \cdots \sum_{\tau_r=\tau_{r-1}}^{M} \right. \right. \\ & \left. \left. \cdot h_{p,r}(0, \ldots, 0, \tau_1, \ldots, \tau_r) \prod_{j=1}^{r} x_{rf}(n - \tau_j) \right] \right\} \end{aligned} \tag{2.24}$$

where P and M denote the order of nonlinearity and memory length respectively. During the regrouping of the parameters based on the order of dynamics, the variable

r is used to represents the dynamics. $h_{p,r}(0,\ldots,0,\tau_1,\ldots,\tau_r)$ is the Volterra kernel with rth-order dynamics and pth-order nonlinearity. The variable r can be adjusted further in real PAs to remove high order dynamics whose effects are insignificant in-terms of contribution to overall nonlinear dynamics.

The classical and DDR-based Volterra series described above use polynomial-type functions, which require wide observation bandwidth when wide bandwidth is employed for radio propagation or when the PA has high order nonlinearity. A bandlimited version of the Volterra series is presented in [20]. It is accomplished by controlling the bandwidth of the Volterra operators using a bandlimiting function before being multiplied by their respective coefficients. The Volterra operator in equation (2.23) is modified by inserting a bandlimiting function $f(.)$ in time domain to yield

$$T_p(x_{rf}(n)) = D_p(x_{rf}(n)) \otimes f(n) \tag{2.25}$$

where $\otimes$ denotes the convolution operation between the bandlimiting function $f(n)$ and classical Volterra operator. After the modification, the bandlimited classical Volterra series is written as

$$\begin{aligned} y_{rf}(n) &= \sum_{p=1}^{\infty}\sum_{\tau_1=0}^{\infty}\cdots\sum_{\tau_p=0}^{\infty} h_{p,BL}(\tau_1,\cdots,\tau_p)T_p(x_{rf}(n)) \\ &= \sum_{p=1}^{\infty}\sum_{\tau_1=0}^{\infty}\cdots\sum_{\tau_p=0}^{\infty} h_{p,BL}(\tau_1,\cdots,i_p)(D_p(x_{rf}(n)) \otimes f(n)) \end{aligned} \tag{2.26}$$

where $f(n)$ is the bandlimiting function with length M, $h_{p,BL}(\tau_1,\cdots,\tau_p)$ is the pth order bandlimited Volterra model parameters. The output $y(n)$ is logically bandlimited since all the Volterra operators are bandlimited, leading to complete bandlimited system, as shown in Figure 2.2. The same modeling operations are applied on a 1-st order DDR-based Volterra series and it results in a bandlimited model. In the expanded form, it can be written as [20]

$$\begin{aligned} y_{env}(n) = &\sum_{p=0}^{(P-1)/2}\sum_{\tau=0}^{M} g_{2p+1,1}(\tau)\left[\sum_{m=0}^{N}|x_{env}(n-m)|^{2p}x_{env}(n-\tau-m)f_{env}(m)\right] \\ + &\sum_{p=1}^{(P-1)/2}\sum_{\tau=1}^{M} g_{2p+1,2}(i)\left[\sum_{m=0}^{N}|x_{env}(n-m)|^{2(p-1)}x_{env}^2(n-m)x_{env}^*(n-\tau-m)f_{env}(m)\right] \end{aligned} \tag{2.27}$$

where the P and M are the nonlinearity order and memory length, respectively.

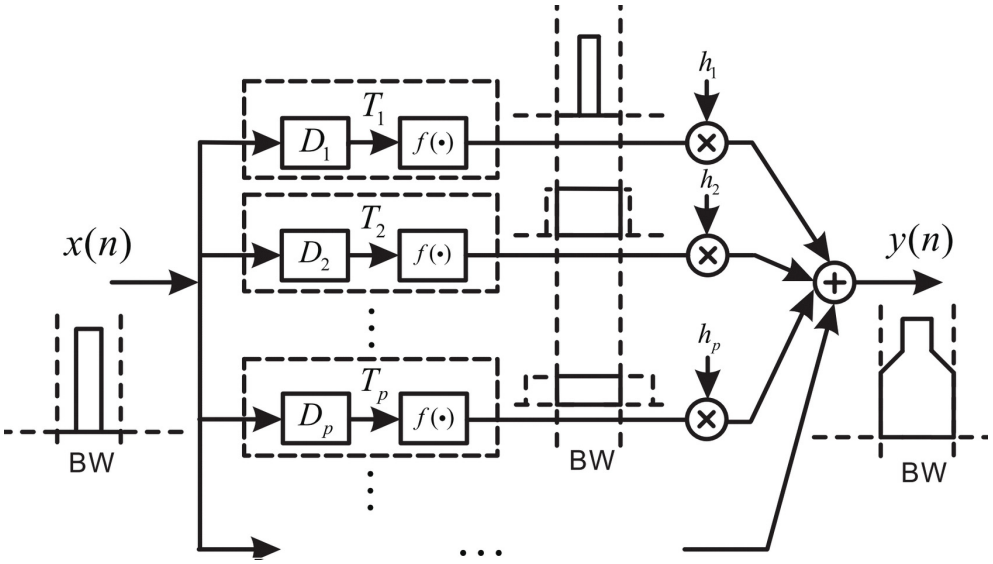

***Figure** 2.2 An Illustration of the band-limited Volterra model in [20]. The Volterra kernels are bandlimited before multiplication with their respective coefficients*

$x_{env}(n)$ and $y_{env}(n)$ denote the complex envelopes of the input and output, respectively, at baseband, while $g_{2+1,j}(.)$ is the complex bandlimited Volterra model parameters.

2.2.2 Memory Polynomial Model

The memory polynomial model is a truncated version of the Volterra series that includes only the diagonal elements [41]. The model is also called the parallel Hammerstein (PH) model. It is widely used for modeling of PAs exhibiting memory effects. The baseband output waveform is given by

$$y(n) = \sum_{j=0}^{M} \sum_{i=1}^{N} a_{\mathrm{ji}} \cdot x(n-j) \cdot |x(n-j)|^{i-1} \tag{2.28}$$

where a_{ji} are the model coefficients while N and M are the nonlinearity order and memory depth, respectively.

There are other variants of the model which have been proposed. One of the widely applied model is the generalized memory polynomial (GMP) model. The model construction involves merging of the memory polynomial model with the cross terms between the signal and the lagging/leading envelope terms. The generalization of the

memory polynomial enables the inclusion of the memory effects caused by transport delays and rapid thermal changes in active devices which affect the signal waveform. The incorporation of these imperfections improve the linearization performance of the model compared to the memory polynomial [42]. The model can be written as

$$\begin{aligned} y_{\mathrm{GMP}}(n) = & \sum_{k=0}^{K_a-1}\sum_{l=0}^{L_a-1} a_{kl}x(n-l)\,|x(n-l)|^k \\ & + \sum_{k=1}^{K_b}\sum_{l=0}^{L_b-1}\sum_{m=1}^{M_b} b_{klm}x(n-l)\,|x(n-l-m)|^k \\ & + \sum_{k=1}^{K_c}\sum_{l=0}^{L_c-1}\sum_{m=1}^{M_c} c_{klm}x(n-l)\,|x(n-l+m)|^k\,. \end{aligned} \tag{2.29}$$

where K_aL_a, $K_cL_cM_c$, and $K_bL_bM_b$ represent the number of coefficients for aligned signal and envelope (which is the case of the memory polynomial), coefficients for signal and leading envelope, and coefficients for signal and lagging envelopes, respectively. The memory polynomial structure is a special case of the model where only the aligned signal and envelope terms are included.

2.2.3 Wiener Model

The Wiener model is a two-box model that is a cascade of a linear dynamic block (FIR or IIR filter) followed a memoryless nonlinearity (usually a polynomial-type function) as shown in figure 2.3. The model input and output signals can be given

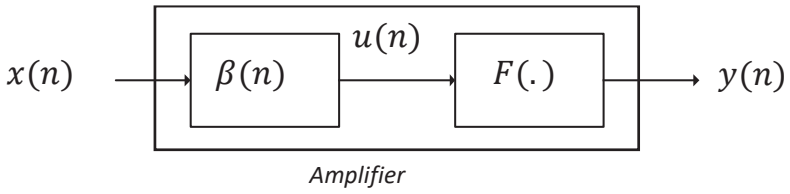

Figure 2.3 *A block diagram of the Wiener model, which is a cascade of a linear dynamic block followed by a memoryless nonlinearity.*

as

$$u(n) = \sum_{\tau=0}^{M} \beta_\tau x(n-\tau) \tag{2.30}$$

and

$$y(n) = F(u(n)) \tag{2.31}$$

where $F(.)$ is the memoryless nonlinearity, and $\beta_\tau(k)$ is the linear dynamic block. As can be seen from equation (2.30), the modeling methodology flouts the identification procedures used in identification of nonlinear systems, hence, it becomes difficult to write the output $y(n)$ explicitly as a function of $x(n)$. This leads to difficulties in parameter estimation and inversion of the equation during linearization.

The linear filter used in the dynamic block is only able to correct electrical memory caused by frequency response of the amplifier. However, it is not sufficient to estimate the impedance disparities due to harmonic loading and bias circuits. As such, another higher order filter is added downstream the wiener model, and system is called the augmented Wiener model [24]. The equation (2.30) now becomes,

$$u(n) = \sum_{\tau=0}^{M} \beta_\tau x(n-\tau) + \sum_{\tau=0}^{M} \beta_\tau x(n-\tau)|x(n-\tau)| \tag{2.32}$$

with equation (2.31) remaining the same.

2.2.4 Hammerstein Model

The Hammerstein model is also a two-box model that is a cascade of a static memoryless nonlinearity followed by a dynamic linear block (IIR or FIR filter). It is similar to the Wiener model with the order of the two blocks reversed as shown in Figure 2.4. The nonlinear static block can written as

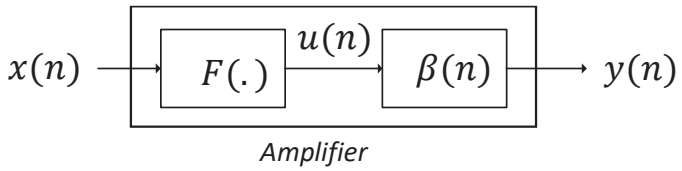

Figure 2.4 *A block diagram of the Hammerstein model, which is a cascade of memoryless nonlinearity and a linear dynamic block.*

$$u(n) = F(x(n)) \tag{2.33}$$

where $F(.)$ is the nonlinear block (usually a polynomial-type function) and $x(n)$ is the input signal. The system output can then be written as

$$\begin{aligned} y(n) &= \sum_{\tau=0}^{M_1} \beta_\tau u(n-\tau) \\ &= \sum_{\tau=0}^{M_1} \beta_\tau F(x(n-\tau)). \end{aligned} \tag{2.34}$$

The concept of the augmented Wiener model is extended to the Hammerstein model giving rise to a dual, the augmented Hammerstein model. As such, another high order filter is added upstream the Hammerstein model. This yields an expression that reads

$$y(n) = \sum_{\tau=0}^{M_1} \beta_\tau F_1(x(n-\tau)) + \sum_{\tau=0}^{M_2} \beta_\tau F_2(x(n-\tau))|x(n-\tau)| \tag{2.35}$$

where $F_1(.)$ and $F_2(.)$ are the nonlinear mappings of the first and second filters, respectively. M_1 and M_2 represent the memory depth of the first and second equations, respectively.

2.2.5 Wiener - Hammerstein Model

The two models are combined together, to form a generalized model, consisting of a linear dynamic block, followed by memoryless polynomial type function and another linear dynamic block. When a signal is inputted, it is first pre-filtered, then nonlinearity is applied, and finally post-filtered to obtain the final output, as illustrated in Figure 2.5. Therefore, there are two intermediate signals, $u_1(n)$ and $u_2(n)$, whose baseband equivalent forms can be written as,

$$u_1(n) = \sum_{\tau=0}^{M_1} \beta_\tau x(n-\tau) \tag{2.36}$$

$$u_2(n) = F(u_1(n)). \tag{2.37}$$

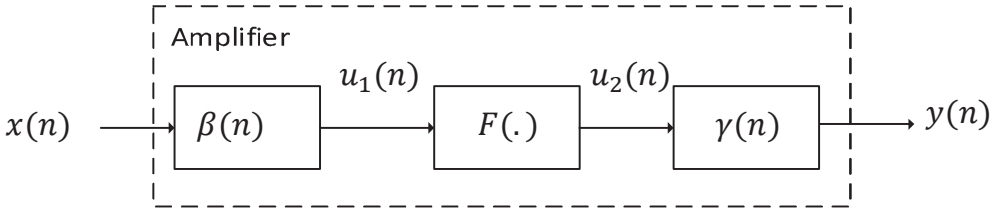

Figure 2.5 *A block diagram of the Wiener-Hammerstein model.*

The final equation, with $x(n)$ as input signal, can now be written as,

$$\begin{aligned} y(n) &= \sum_{i=0}^{M_1} \gamma_i u_2(n-i) \\ &= \sum_{i=0}^{M_1} \gamma_i F(u_1(n-i)) \end{aligned} \tag{2.38}$$

2.2.6 Saleh Memory-Based Model

This is the frequency dependent version of the Saleh model, and is used on frequency selective channels (this is usually the case when wideband input signals are applied on the PA). The parameters α_a, α_Θ, β_a, and β_Θ in equation(2.14) become frequency selective, and the input/output in-phase and quadrature signal conversions now read,

$$S_I(A,w) = \frac{\alpha_a(f)A}{1+\beta_a(f)A^2} \tag{2.39}$$

$$S_Q(A,w) = \frac{\alpha_b(f)A^3}{(1+\beta_b(f)A^2)^2} \tag{2.40}$$

where S_1 and S_Q are the in-phase and quadrature signal mappings, respectively.

2.3 Discussion

In this chapter, both the memoryless and memory-based PA models have been discussed, with emphasis put on the formulation and representation of PA nonlinearity in equations and block diagrams. The memoryless models have less parameters and

are easy to identify and formulate. However, they may not accurately represent the performance of the PA since they don't factor in crucial non-idealities in the real operating environment. Moreover, wideband power amplifiers exhibit frequency dependent behavior and therefore frequency selective response. Memory-based PA models are adopted in most simulation-level environments because they don't only represent the frequency selective behavior but also memory and electrical effects, which may cause significant influence of the PA model parameters.

In the discussions, however, the issue of identification complexity has not been dealt with comprehensively. The detailed analysis of the models' identification complexity in FLOPS has been in done[17], with the corresponding linearization performance on different commercial PAs being reported also. For instance, the GMP model was shown to have the highest accuracy vs. FLOPS at the lowest computational cost followed by the PH model when evaluated using the widely used Doherty amplifier. The Volterra series offers the best performance in all the PA scenarios when the complexity perspective is not considered.

3. EFFECTS AND MITIGATION OF POWER AMPLIFIERS NONLINEARITY

Power amplifiers are inherently nonlinear, and therefore negatively affect the performance of the entire analog front-end by causing RF impairments. The alleviation of the PA nonlinearity is essential in preserving the integrity of the information in the transmitted signal and reducing the interference and cross-talk with the adjacent channels. These adverse effects include inband distortion, adjacent band interference, and distortion of the signal envelope in QAM modulation scheme. The enhancement of PA linearity enables the use of very dense signal constellations, which translates to higher spectral efficiency. Moreover, PA power efficiency is highly desirable to achieve maximum coverage when the operation is near the saturation region.

In this chapter, we will start by analyzing the effects of the power amplifier nonlinearity on single tone and multitone communication signals. In particular, the effects of harmonic and intermodulation (IMD) components on the PA input signal characteristics will be presented. In the other sections, the widely used analog and digital linearization methods are explored, with emphasis put on digital predistortion.

3.1 Effects of Power Amplifier Nonlinearity

The PA has a nonlinear profile, hence it distorts the input signal by introducing unwanted emissions in the inband (in the occupied transmit band), out of band (OOB), and spurious regions. The OOB emissions are in the adjacent bands next to the main carrier, and are defined in terms of the ACLR and spectral mask [1]. The spurious emissions occupy other parts more far away in the spectrum and are also caused by harmonic and intermodulation products.

In this analysis, we use a two-tone signal to demonstrate the introduction of unwanted emissions by a PA using a third order memoryless polynomial-type nonlinear

system. The nonlinear system is given by

$$y = a.x_{in} + b.x_{in}^2 + c.x_{in}^3 \tag{3.1}$$

where y and x_{in} are the output and input signals, respectively, while a, b, and c are the system nonlinear coefficients. The input signal x_{in} is a two-tone signal given by

$$x_{in}(t) = A_1.\cos(w_1 t) + A_2.\cos(w_2 t) \tag{3.2}$$

where A_1 and A_2 magnitudes of the two signals, and w_1 and w_2 are the angular frequencies of the two signals with $w_2 > w_1$.

By combining equations (3.1) and (3.2), the output signal becomes [43]:

$$\begin{aligned}
y = & \underbrace{\left[\frac{1}{2}bA_1^2 + \frac{1}{2}bA_2^2\right]}_{\text{DC component}} \\
& + \underbrace{\left[\left(a + \frac{3}{4}cA_1^2 + \frac{3}{4}cA_2^2\right).A_1.\cos(w_1 t) + \left(a + \frac{3}{4}cA_2^2 + \frac{3}{4}cA_1^2\right).A_2.\cos(w_2 t)\right]}_{\text{amplified fundamental frequencies(wanted signal)}} \\
& + \underbrace{\left[\frac{1}{2}bA_1^2\cos(2w_1 t) + \frac{1}{2}bA_2^2\cos(2w_2 t)\right]}_{\text{second order harmonics}} + \underbrace{\left[\frac{1}{4}cA_1^3\cos(3w_1 t) + \frac{1}{4}cA_2^3\cos(3w_2 t)\right]}_{\text{third order harmonics}} \\
& + \underbrace{[bA_1A_2\cos((w_2 - w_1)t) + bA_1A_2\cos((w_2 + w_1)t)]}_{\text{second order IMDs}} \\
& + \underbrace{\left[\frac{3}{4}cA_1^2A_2\cos((2w_1 - w_2)t) + \frac{3}{4}cA_1A_2^2\cos((2w_2 - w_1)t)\right]}_{\text{in-band third order IMDs}} \\
& + \underbrace{\left[\frac{3}{4}cA_1^2A_2\cos((2w_1 + w_2)t) + \frac{3}{4}cA_1A_2^2\cos((2w_2 + w_1)t)\right]}_{\text{OOB third order IMDs}}.
\end{aligned} \tag{3.3}$$

From equation (3.3) and as illustrated in Figure 3.1, it is clear that there are unwanted emissions (frequency components) that have been introduced to the output signal. The resultant frequency components can be broadly classified into three groups [43]:

- *The useful/wanted signal.* This is the linearly amplified signal comprising of the fundamental frequency components, w_1 and w_2.

- *Unwanted signals removable by filtering.* In addition to the useful signal, there are other frequency components, i.e DC component, second order harmonics and intermodulation products (IMDs), and third order harmonics and OOB IMDs, which fall in the spurious domain. They are far from the fundamental frequencies and are easily removed by RF filtering.

- *Unwanted signals that are not removable by filtering.* These are the signal components that fall directly on top or in the immediate vicinity of the main frequency components. It is infeasible to filter out these components since it requires a high order filter, which increases the processing complexity.

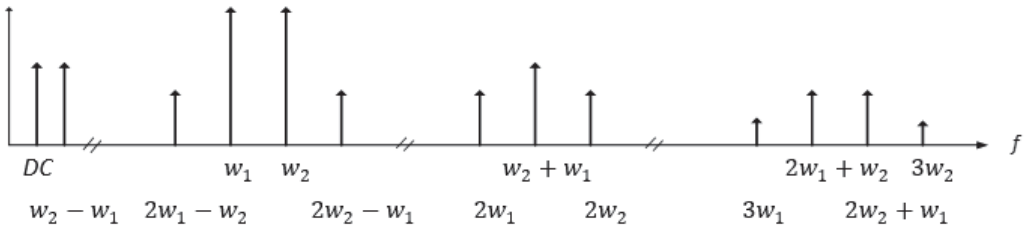

Figure 3.1 *Frequency domain output of a third-order nonlinear system driven by two-toned signal.*

The above analysis can be extended to predict the nonlinear behavior of multi-tone signals such as OFDM signals where many sub-carriers are closely spaced, and in continuous spectrum signals. This is illustrated in Figure 3.2, and shows the spectral regrowth which falls both on the spurious and OOB domains.

The PA nonlinearity is detrimental in modern communication systems which employ high order complex modulation schemes (e.g. 64 QAM and 256 QAM) and advanced multiplexing schemes (e.g. OFDM). The resultant transmit signals have high envelope fluctuations which falls in the nonlinear region of the amplifier. The high signal variations are characterized by the PAPR, calculated as

$$PAPR_{dB} = 10 \log \left(\frac{P_{max}}{P_{avg}} \right) \tag{3.4}$$

where P_{max} and P_{avg} are the signal's peak and average power levels, respectively. The operating PAPR of most communication systems is 10 - 13 dB, and therefore there

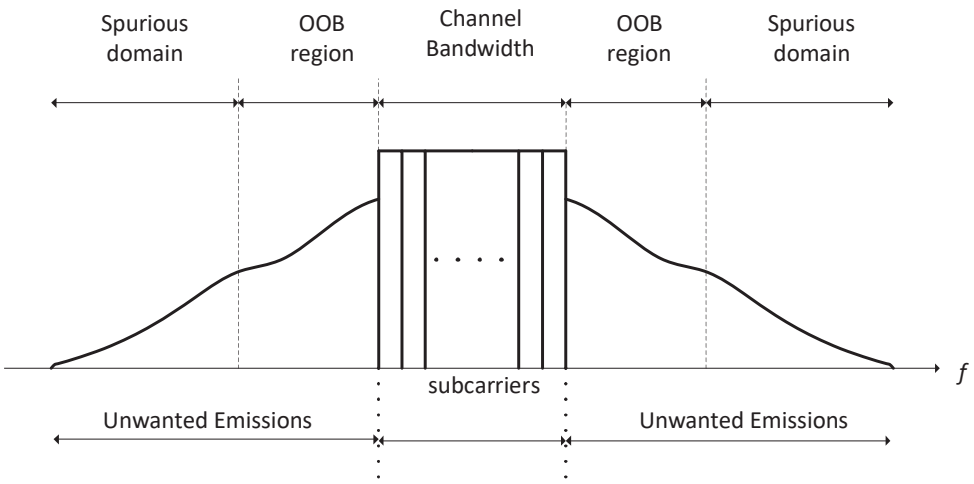

Figure 3.2 *Transmitter spectrum of a multicarrier signal. The PA output contains spectral regrowth and occupies both the spurious and OOB domains.*

is need to lower the high envelope fluctuations to achieve the linear amplification. Different methods of lowering the PAPR have been proposed in [44, 45, 46]. The power amplifier efficiency is jointly improved by slightly reducing the PAPR and using a PA linearization scheme, which ensures the PA operates near the saturation point and the gain expansion capabilities of the linearization scheme are leveraged. In the next section, the different approaches employed for linearization are discussed.

3.2 Feedback Linearization

Feedback linearization is one of the simplest method of mitigation of PA nonlinearity and uses a feedback loop for error cancellation. The principle of operation is to extract the error signal from the output signal by comparing it with the input signal, and then injecting it back to the PA with opposite phase [47]. The method is widely used for amplification of narrowband signals, such as in audio amplifiers. A basic feedback system is shown in Figure 3.3. It has a comparator for calculating the error signal from the input signal and the signal from the feedback path. The feedback system is able to compensate the error signal when the bandwidth involved is small (in kHz range), however, error cancellation becomes problematic when the signal bandwidths are wide.

Several methods have therefore been proposed to overcome this challenge. They include the Cartesian modulation feedback, and envelope feedback, among others.

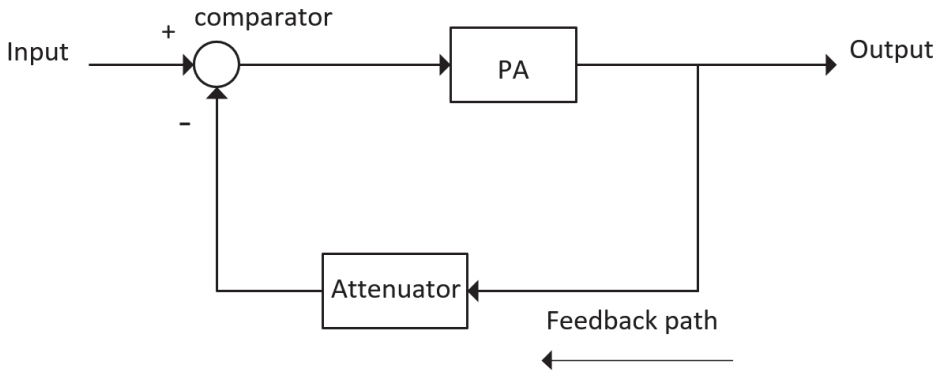

Figure 3.3 *A basic structure of a feedback system.*

The Cartesian feedback involve two loops, one for the in-phase component and other for the quadrature component. The feedback signal is down-converted to baseband and the error computation is done separately for the I and Q components. The processing of the signals at baseband eliminates the delay synchronization problems because of the slow variations of the baseband equivalent signal.

In the envelope feedback in [48], only the envelope of the signal is detected and corrected. Envelope detectors are employed at the feedback loop and signal generator, and a comparison of the two signals is done. The resultant signal is then fed to a gain controller via a low pass filter. Figure 3.4 shows a basic envelope feedback system, where an envelope generator and detector are used for mitigation of PA nonlinearity for an I/Q signal source.

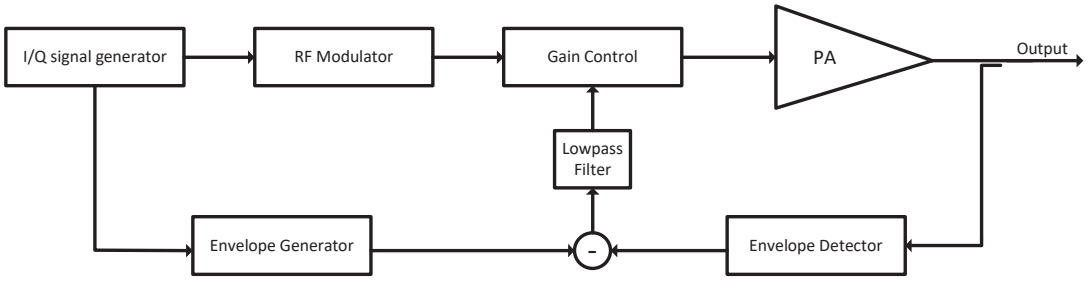

Figure 3.4 *A simplified structure of an envelope feedback system.*

3.3 Feedforward Linearization

The linearization is done by obtaining the output signal of the amplifier and identifying the distortions in the signal, and then doing the distortion cancellation after the PA. A typical circuit of a feedforward linearizer is shown in the Figure 3.5. This involves the implementation of two loops, one for signal cancellation (SCL) and the other for error cancellation (ECL). The SCL is used for identification of

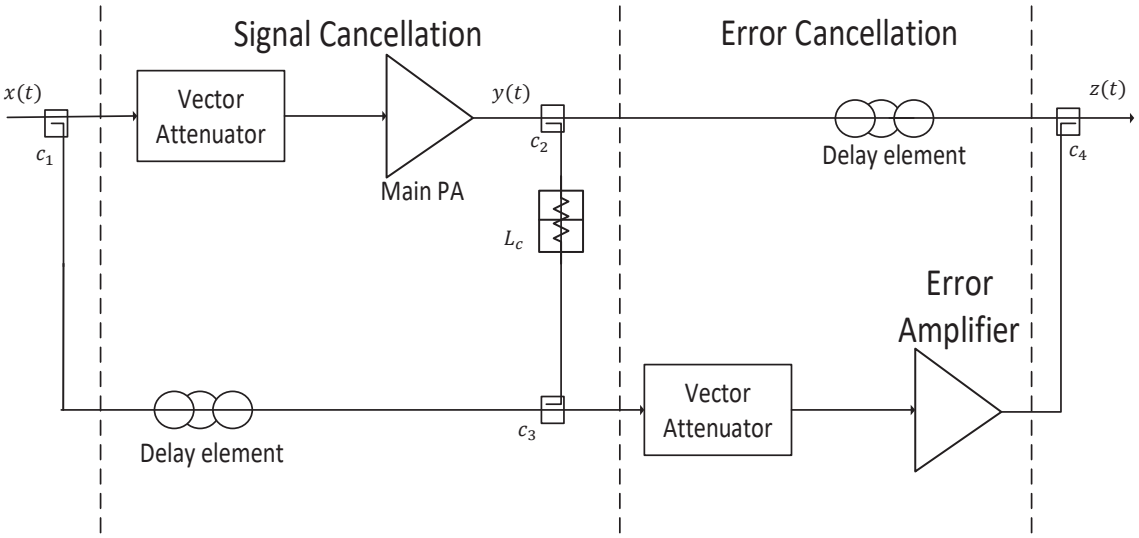

Figure 3.5 *A block diagram of a feedforward linearization system and its essential components.*

the distortions caused by the PA. The input signal is separated by a coupler C_1 into two branches, an upper branch where signal is fed to the PA, and a lower branch where the signal goes through a delay circuit before been coupled with an attenuated output signal from the PA. The attenuator L_c and the delay element ensure that the signals at the inputs of the coupler C_3 have same power level and are synchronized, respectively. The coupler C_3 yields an error signal $e(t)$ which is the difference between the synchronized output and the input signals, and contains the signal distortion caused by the PA.

The error signal $e(t)$ and the coupled output signal are then fed to the ECL loop, which does the cancellation of the error signal. The error signal $e(t)$ is passed through a vector attenuator for scaling and phase tuning before been amplified to

the power level of the signal in the upper branch. The amplification is necessary to ensure both upper and lower branches have the same power level for effective cancellation. The upper and lower branches signals are injected to the coupler C_4 which cancels the error and yields a distortionless signal $z(t)$.

However, the whole cancellation system is suspectible to variation in operating conditions and coefficient mismatch in the ECL and SCL loops when adaptive algorithms are applied. Besides, phase and gain matching between all the circuit elements must be maintained at high accuracy for the error cancellation to be effective [49].

3.4 LINC

LINC is an acronym for linear amplification with nonlinear components. The method involves the splitting of the signal into two constant envelope signals whose sum yields the original signal [50]. The two signals are then passed separately through normal power amplifiers and their outputs combined to form the transmit signal. The transmit signal is free from any nonlinearity since the AM/AM and AM/PM mappings are flat due to the linear amplification of the constant envelope signals. Harmonic components originating from the nonlinear amplifiers are easily suppressed by a low pass filter. The LINC system is illustrated in Figure 3.6.

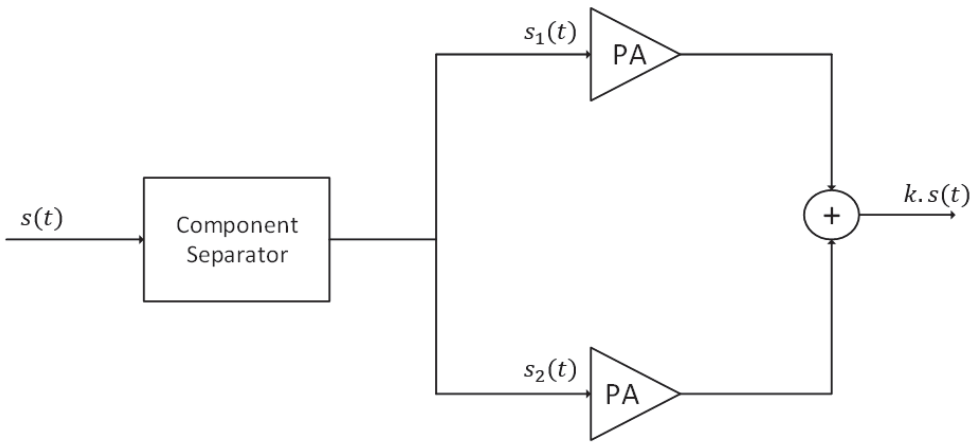

Figure 3.6 *A simplified Linearization structure using the LINC Concept.*

A general baseband equivalent signal flow through the LINC system is analyzed

below. A baseband signal can written as,

$$s(t) = A(t).\cos(wt + \phi(t)) \tag{3.5}$$

The two constant envelope signals are derived from equation (3.5) and are written as,

$$s_1(t) = \frac{a_{max}}{2}.\cos(wt + \alpha(t)) \tag{3.6}$$

$$s_2(t) = \frac{a_{max}}{2}.\cos(wt - \alpha(t)) \tag{3.7}$$

where a_{max} is maximum amplitude of $A(t)$. To obtain a linearly amplified version of the original signal from the sum of the two equations, the phase of the signals $\alpha(t)$ should be defined as,

$$\alpha(t) = \cos^{-1}\left(\frac{A(t)}{a_{max}}\right) \tag{3.8}$$

The LINC method suffers from a major drawback in power combining after the PAs due to difficulties in component separation, and subsequent synchronization and combining of the two signals after amplification. When the two signal are uncorrelated, the combining results in a 3 dB insertion loss which degrades the performance of the entire system [51].

3.5 CALLUM

CALLUM is the abbreviation for combined analogue locked loop universal modulator. It uses same operating principle as the LINC system but the constant envelope signals are generated by combining the I and Q components of the input signal separately with signals obtained from a feedback loop [52]. The feedback receiver signal is demodulated and each of the I/Q components is compared with the respective input components to form the error signals. The error signals are fed to a voltage controlled oscillator (VCO) and then to the PA, producing a high gain loop. The phase and gain of the transmitter are precisely controlled by the feedback loop ensuring the error signal is minimized. Figure 3.7 shows a basic CALLUM structure.

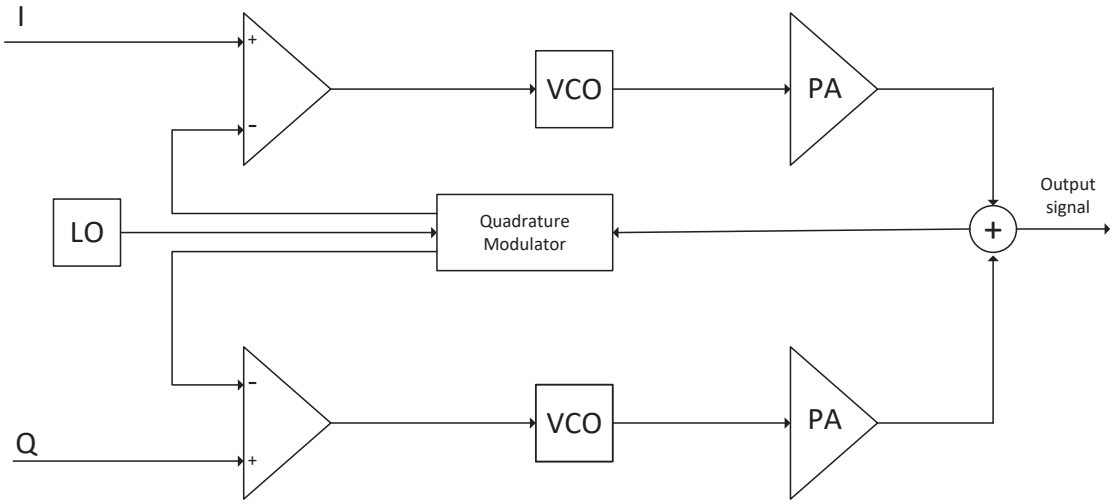

Figure 3.7 *A simplified Linearization structure using CALLUM Principle.*

3.6 Digital Predistortion

Digital predistortion is the application of the inverse nonlinearity of the main PA (predistorter) at digital baseband such that the cascade of the overall system has a linear gain [24]. In designing a predistorter, the accuracy of the behavioral model function used plays a major role in the successful reversal of the PA nonlinearity as the distortion is represented using a PA model. Predistortion can be done at the transmit signal at any of the signal processing stages; at baseband, at intermediate frequency (IF), or at radio frequency (RF). Figure 3.8 shows a simplified digital predistorter operating at baseband frequency.

Due to the aging effects and inevitable environmental changes, the predistorter performance may deteriorate over time. These adverse effects can be overcome by periodically tracking the PA changes and updating the predistorter function. Adaptive digital predistortion algorithms have been proposed in [43, 53], and mostly operate at baseband or low-IF frequencies. In the following subsection, we shall discuss the widely used digital predistorter adaptation algorithms from the implementation and design perspectives.

3.6.1 Direct Learning Architecture

In the direct learning method, the PA model is first identified and then the predistorter equation is computed by inverting the PA model of the amplifier. The

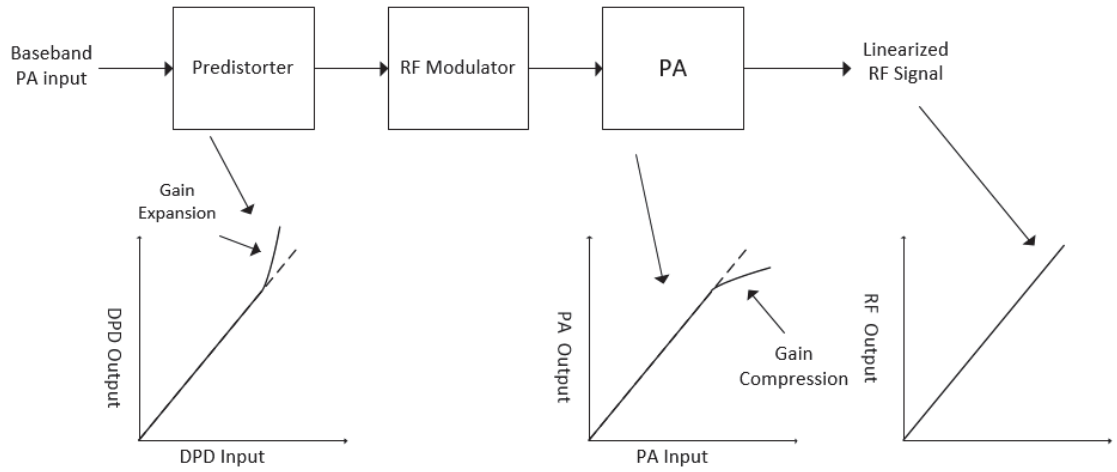

Figure 3.8 *A functional block diagram of Baseband DPD Linearization system and corresponding gain characteristics of predistorter and PA. The gain expansion at the predistorter compensates the gain compression exhibited by the PA resulting in a linearized RF output.*

predistorter is updated with the computed inverse equation. The method is easily applicable to memoryless PA models/systems where the instantaneous input and output AM/AM and AM/PM mappings exist. In memory-based PA models and systems, the PA function inversion becomes much more complicated [54]. Figure 3.9 illustrates a direct learning architecture, where PA model is computed before inversion is done.

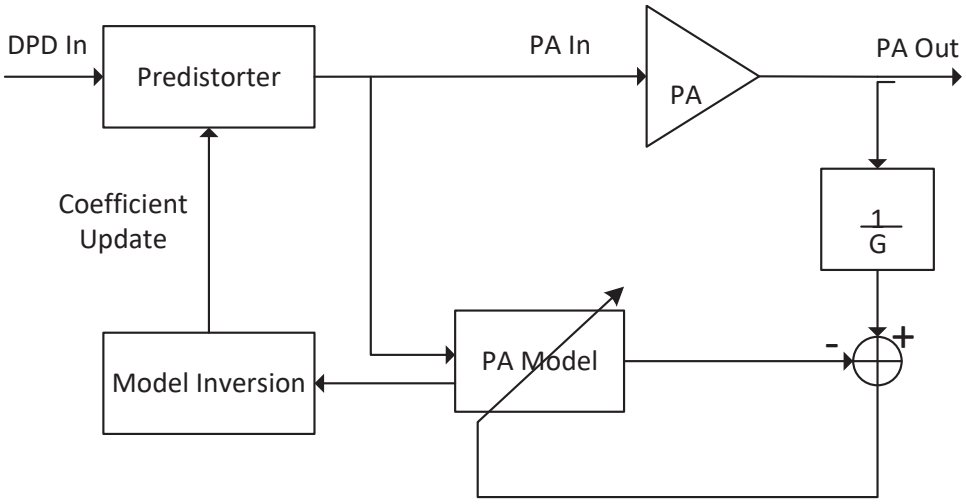

Figure 3.9 *Direct learning Architecture.*

3.6.2 Indirect Learning Architecture

The indirect learning algorithm is developed to ease off the complication and errors experienced in the DPD function inversion. The post-inverse of the PA is first identified by interchanging the input and the output signals, and the resultant function is used as the predistorter function upstream.

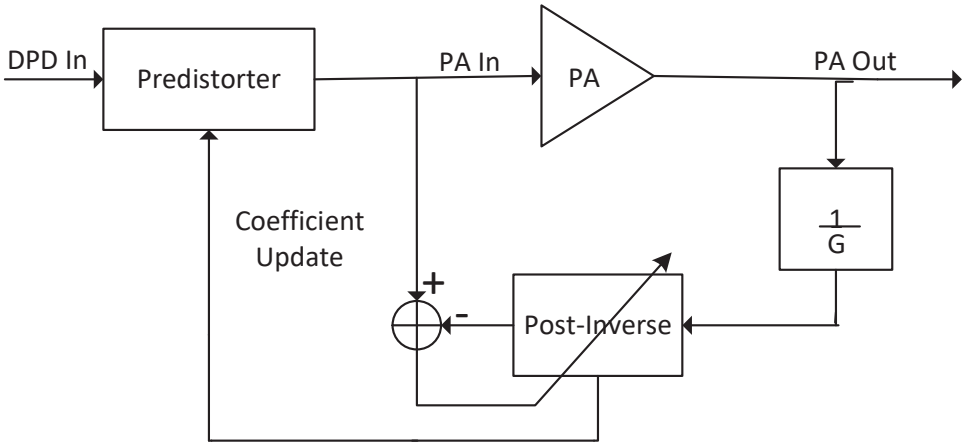

Figure 3.10 *Indirect learning Architecture.*

However, the system suffers from reduced power range due to the interchanging of the input and output during calculation of the post-inverse. This limits the operation of the amplifier up to a particular input power level below the saturation point.

3.6.3 Closed Loop Adaptive Digital Predistortion

The predistorter is inside the feedback adaptation loop that is used for parameter update. Figure 3.11 illustrates the closed loop block diagram, where the input and output signals of the PA are used to calculate the error signal, which is used by the adaptive algorithm to update the parameters to be fed to the predistorter. In this method, the distortion signal is minimized in subsequent loops until convergence is achieved. Furthermore, the closed loop estimation and update is less sensitive to noisy feedback observations compared to the direct and indirect learning architectures discussed in the previous sections [55].

In Chapter 4, the closed loop decorrelation-based method is used for parameter learning.

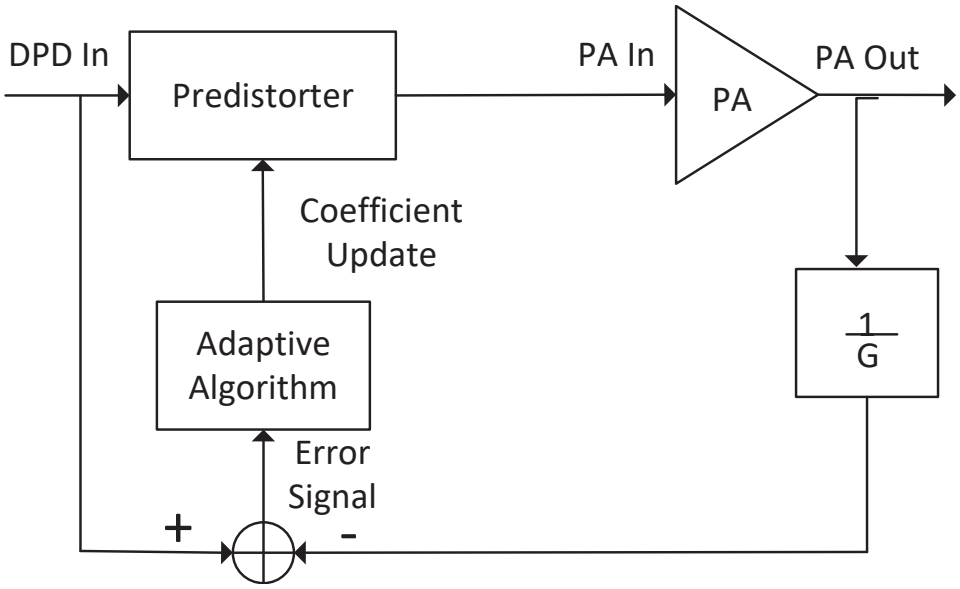

Figure 3.11 *Closed Loop Adaptive learning Architecture.*

3.7 Discussion

PAs are nonlinear devices that cause significant RF imperfections on the transmit signal. Among the negative effects of the nonlinear behavior of the PA are distortion of the signal envelope, adjacent channel interference, and the introduction of inband waveform impurities. The introduction of the nonlinear distortions by the PA has been exemplified using a two-tone signal applied to a third order nonlinear system. The unwanted frequency components introduced can be classified into three groups namely; inband distortion, OOB distortion, and spurious emissions.

The spurious emissions are more far in the spectrum from the input signal and can be suppressed using the transmit or cavity filters, while inband and OOB emissions require the use of alternative methods for cancellation. The alternative methods developed include the feedback linearization, feedforward linearization, LINC, CALLUM, and digital predistortion, among others. The above methods cancel the PA nonlinearity significantly when operated near saturation (with minimum power back-off), hence enhancing power efficiency. This effectively allows the use of high-order dense constellations, thus improving spectral efficiency. The above methods, however, have their shortcomings in terms of the complexity, adaptation to environmental changes, linearization performance, and applicability in modern communication systems. In this light, the selected linearization method should provide the best tradeoff among

the above competing interests in a communication system.

4. BANDLIMITED DIGITAL PREDISTORTION

In this chapter, we introduce and analyze the concept of bandlimited predistortion in continuous transmit spectrum or contiguous CA of two or more CCs. In both mobile handsets and base station transmitters, the need to linearize the inband and adjacent spectral distortions caused by the nonlinear amplifiers is becoming extremely important due to the increasing bandwidth allocations of the transmit signal to accommodate higher data rates while still ensuring power efficiency [1]. This has, however, become strenuous to the entire transmitter chains due to the increasing number of computations and high speed converters required for signal processing. For instance, there is an increase in the sample rates required for ADC and nonlinearity observation in the feedback receiver. The increased complexity in system design may make DPD linearization infeasible for wide bandwidth allocations proposed for future LTE-A implementations.

For wide bandwidth allocations, the suppression of inband distortion and spectral regrowth can be done in two ways: First, the inband distortion and spectral regrowth in the very near vicinity of the transmit band can be linearized using DPD, and the spectral regrowth more far from the main carrier(s) are filtered out using a bandpass filters at the PA output or cavity filters in duplexers of FDD transceivers. The proposed approach yields the following benefits [56]:

- There is a significant reduction in the bandwidth required for PA feedback observation, in that only a fraction of the PA nonlinearity is observed for linearization using DPD. This consequently reduces the sample rate of the ADC in the feedback path.
- The bandlimited DPD solution offers an extra degree of freedom in the linearization of PA nonlinearity. The extent of the bandwidth to be linearized can be chosen using a bandlimiting function based on the nonlinearity suppression needed and the nonlinearity profile of a PA. This is particularly simple since the bandlimiting filtering is done in the discrete-time domain.

- The filtered basis functions used in the proposed DPD solution are generated using lower sample rates and computational cost compared normal basis functions in conventional DPD methods.

We start by analyzing the signal processing of baseband equivalent signal and the effects of sample rates used in DPD processing in mitigating the PA nonlinearity. Thereafter, we develop a distortion component model where we formulate the PA nonlinearity and the SNL basis functions to be used for DPD learning and parameter update. We finalize the chapter by analyzing the parameter update algorithms employed namely, the sample and block closed-loop decorrelation-based learning.

4.1 Basics of Sampling and Filtering Theory

In digital communication systems, signal generation is done in time domain and then digitally modulated into in-phase and quadrature (I/Q) components for RF transmission. Modern radio systems use the direct-conversion transceiver architecture which involves the use of complex I/Q signal processing for baseband to RF frequency conversion. The frequency translation is done by multiplying the signal with a complex-valued signal from a numerically-controlled oscillator whose frequency is the centre frequency of the allocated channel band in spectrum.

The input signal is resampled to a higher sampling rate depending the transmission and predistortion requirements of the system. For instance, for LTE-A signal with a bandwidth of 20 MHz, the signal generation is done at 30.72 mega-samples per second (MSa/s) and then upsampled by 4 or 5 times to yield a DPD sample rate of 122.88 MSa/s or 153.6 MSa/s, respectively, to accommodate the PA nonlinearity and predistorter observation path [1]. However, the required five time over sampling rate may not be sufficient to capture all the PA nonlinearity when the PA is driven near saturation. Operating the PA near saturation requires that a higher order behavioral model is adopted, usually a 11^{th}- or 13^{th}- degree nonlinearity, to obtain all significant spectral distortions [53]. Otherwise, the simulation results may not be valid when real PA implementations are done.

The upsampling of the I/Q signals is performed to increase the sample rates since the predistorter increases the bandwidth requirement of the PA input signal to ensure linearization occurs in the adjacent bands. In case the expanded bandwidth is less than the PA nonlinearity profile, aliasing is bound to occurs to the side-bands

of the PA output signal, and therefore the feedback observation receiver signal will be corrupted, affecting the overall performance of the predistorter. Likewise, undersampling will also have the same effect on the linearization performance, making it impossible to recover the transmitted signal by resampling at the PA output. Hence, the sample rates adopted should accommodate the PA nonlinearity profile as well as the DPD bandwidth requirements. Figure 4.1 shows the effects of undersampling and oversampling.

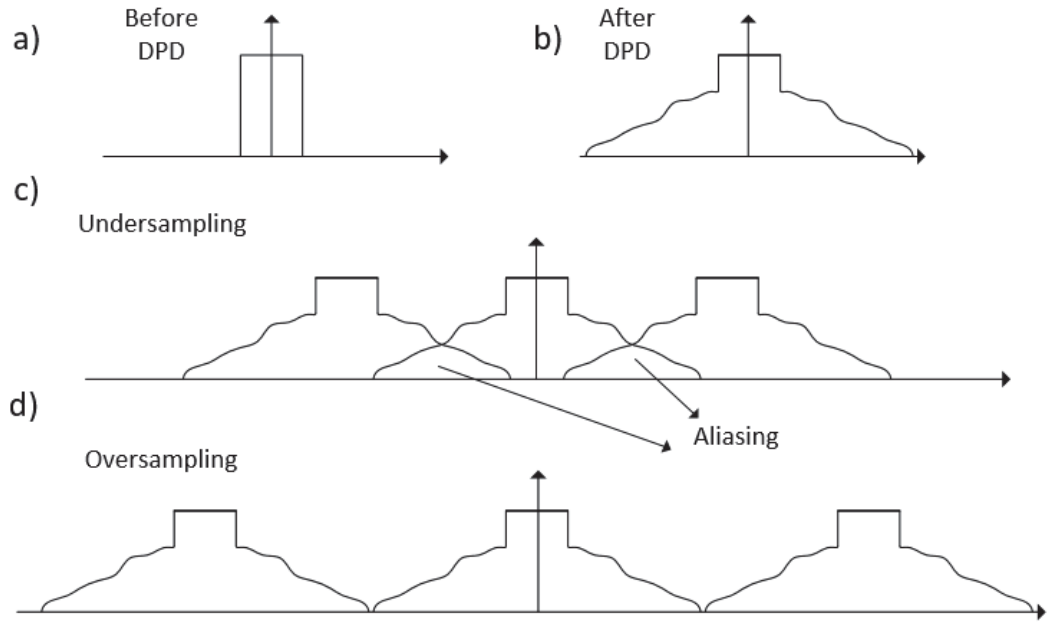

Figure 4.1 *The effects on sampling rates of the DPD signal. The predistorted signal (b) has a wider bandwidth than the original signal (a). Low sampling rates leads to undersampling in (c) resulting in aliasing of the side-bands, hence the original signal cannot be recovered thereafter. Oversampling prevents aliasing as is the case in (d).*

The sample rates required to accommodate high degree nonlinearity are usually very high especially when the signal is transmitted using wide bandwidths. In scenarios where high data rates are highly desirable and necessary, the deployment of one or more component carriers (CCs) with a resultant bandwidth of more than 20 MHz would require very wide channel bands to capture the entire nonlinearity profile for highly nonlinear amplifiers. This would increase sample rates to exhobitant levels, and further escalate the hardware requirements for the DACs and ADCs.

The above implementation problem can be mitigated by using the bandlimited con-

cept introduced in [20] and [21] by limiting the band to be linearized using a bandlimiting function. A bandlimited Volterra-series is proposed in [20] (explained in subsection 2.2.1) to limit the expansion of the bandwidth during behavioral modeling by bandlimiting the input and output signals. This is later applied in [21] for DPD linearization of different implementation scenarios for contiguous and noncontiguous CA of two or more CCs allocations. The performance of the these systems is evaluated and excellent suppression of the inband distortions and OOB (in the linearized bandwidth) distortions is reported in all the scenarios. In this thesis, we extend the bandlimiting concept by introducing a filtering function to reduce the DPD running bandwidth (i.e., by bandlimiting the bandwidth of the PA feedback observation signal and the basis functions bandwidth), thereby preventing aliasing from occurring when lower sample rates are employed, as depicted in Figure 4.2.

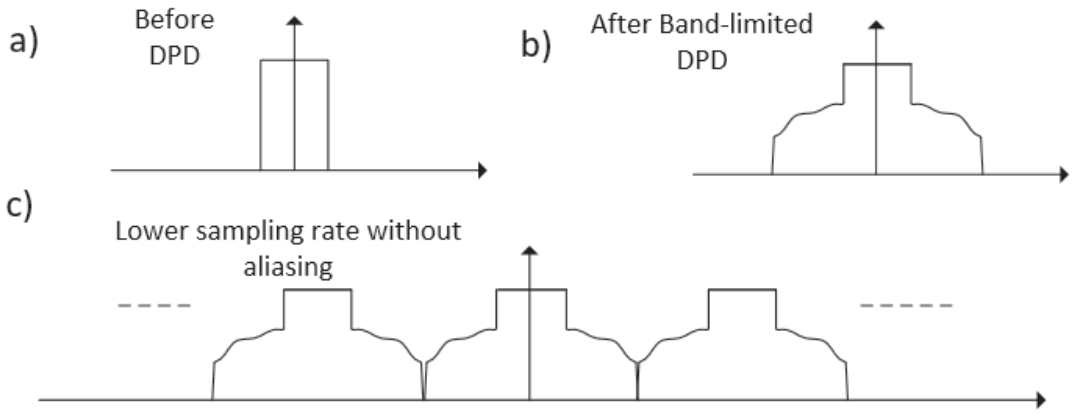

Figure 4.2 *The effect of bandlimiting the DPD output on the sampling rate. Bandlimiting reduces the bandwidth occupied by the predistorter signal and hence lower sampling rates can be employed without aliasing occuring.*

In the implementations, the computational cost of the bandlimiting functions is not evaluated, and the subsequent effect on the inband and OOB suppression is also not analyzed. A tradeoff between the computational cost of multiplying the input and output signals with bandlimiting function(s) and the DPD suppression performance is inevitable. The higher the order of the bandlimiting functions, the higher the nonlinearity suppression. However, there is a resultant increase in the computational cost of doing the filtering. The quantitative performance tradeoff is analyzed through simulations and RF measurements in Chapter 5.

4.2 Digital Predistortion Modeling

In this section, practical cases of a single CC or contiguous CA of two or more CCs is assumed for the signal modeling. The input signal to the PA and will be denoted by $x(n)$ in both scenarios for simplicity and without loss of generality. The inband distortion and spectral regrowth around the carrier are modeled, and the bandlimited concept introduced in our analysis.

The bandlimited concept in [20] is applied in our analysis and used for filtering the basis functions and feedback receiver observation signal in the DPD processing block. This concept is also employed in [56] and excellent suppression of PA nonlinearity and other RF front-end imperfections (I/Q imbalance and LO leakage) is reported. In the analysis, we restraint the DPD parameters to a band defined by the limiting function, rather than bandlimiting the behavioral model input and output signals as is the case in [21].

4.2.1 Basis Functions Generation and Orthogonalization

The SNL basis functions are employed in the predistorter to represent the PA nonlinearity/distortion and are used for identification and formulation of the predistortion functions. The basis functions are generated in a similar manner as the PA behavioral models. In the modeling, we adopt the parallel Hammerstein (PH) model in [19], which has been shown to represent different classes of PAs accurately and at a low computational cost [17], and it reads,

$$u_p(n) = x(n)|x(n)|^{p-1} \tag{4.1}$$

where p is the nonlinearity order of the basis functions, and $x(n)$ is the composite baseband equivalent input signal. The basis functions, assuming the 9^{th}-order PA model, now read

$$u_3(n) = x(n)|x(n)|^2 \tag{4.2}$$
$$u_5(n) = x(n)|x(n)|^4 \tag{4.3}$$
$$u_7(n) = x(n)|x(n)|^6 \tag{4.4}$$
$$u_9(n) = x(n)|x(n)|^8. \tag{4.5}$$

The basis functions are strongly correlated among themselves and with the input signal and thus susceptible to numerical instability, which may compromising the proposed DPD solution performance [14, 57]. This can negatively affect the parameter update process since the adaptive decorrelation-based learning takes place concurrently for all nonlinearity orders. Hence, there is a clear need for basis functions orthogonalization for smooth and fast convergence. The basis functions orthogonalization is done sequentially using the Grad-Schmidt orthogonalization, starting with the third-order basis functions, and a new set of basis functions are obtained, and they read,

$$v_3(n) = u_3(n) - \frac{dot(u_3(n), x(n))}{\|x(n)\|^2} x(n), \tag{4.6}$$

$$\begin{aligned} v_5(n) = u_5(n) &- \frac{dot(u_5(n), x(n))}{\|x(n)\|^2} x(n) \\ &- \frac{dot(u_5(n), v_3(n))}{\|v_3(n)\|^2} v_3(n), \end{aligned} \tag{4.7}$$

$$\begin{aligned} v_7(n) = u_7(n) &- \frac{dot(u_7(n), x(n))}{\|x(n)\|^2} x(n) \\ &- \frac{dot(u_7(n), v_3(n))}{\|v_3(n)\|^2} v_3(n) \\ &- \frac{dot(u_7(n), v_5(n))}{\|v_5(n)\|^2} v_5(n), \end{aligned} \tag{4.8}$$

$$\begin{aligned} v_9(n) = u_9(n) &- \frac{dot(u_9(n), x(n))}{\|x(n)\|^2} x(n) \\ &- \frac{dot(u_9(n), v_3(n))}{\|v_3(n)\|^2} v_3(n) \\ &- \frac{dot(u_9(n), v_5(n))}{\|v_5(n)\|^2} v_5(n) \\ &- \frac{dot(u_9(n), v_7(n))}{\|v_7(n)\|^2} v_7(n). \end{aligned} \tag{4.9}$$

The above functions can alternatively be obtained through, for example, QR decomposition, singular value decomposition, or LU decomposition.

4.2.2 Basis Functions and Receiver Feedback Filtering

The orthogonalized basis functions and the receiver observation signal are further processed to lower the learning computational complexity by reducing the sample rates required in the DPD adaptation. This is done by filtering and decimating the

basis functions and feedback receiver signal with a lowpass filter f_n whose bandwidth is less than the bandwidth occupied by the maximum nonlinearity order of the PA model. The orthogonalized basis functions and receiver feedback signal are therefore transformed into bandlimited functions, and occupy bandwidth defined by the filter f_n, and they read,

$$s_3(n) = f_n \otimes v_3(n) \tag{4.10}$$

$$s_5(n) = f_n \otimes v_5(n) \tag{4.11}$$

$$s_7(n) = f_n \otimes v_7(n) \tag{4.12}$$

$$s_9(n) = f_n \otimes v_9(n) \tag{4.13}$$

where $\otimes$ denotes the convolution operator, and s_3, s_5, s_7, and s_9 denotes the filtered-orthogonized basis functions. The feedback observation signal is also filtered using the same lowpass filter f_n used for the basis functions, and is then used to calculate the nonlinear distortions introduced by the PA as follows [56]

$$e(n) = [f_n \otimes y(n)/G] - x(n) \tag{4.14}$$

where $e(n)$ is the nonlinear distortion, $y(n)$ is the PA baseband equivalent output signal, and G is the estimated complex linear gain calculated using simple estimation techniques, such as the least squares method. The nonlinear distortion signal and filtered-orthogonalized basis functions are used in the next section to estimate the DPD filter coefficients and the computation of the predistorter function.

4.2.3 Distortion Components Modeling

The DPD system is designed to inject a low-power cancellation signal to the transmit signal such that the PA output signal distortions are substantially reduced and the signal linearity is restored. The DPD learning and parameter update is carried out at baseband equivalent level, and hence the feedback signal is down-converted before been bandlimited using a lowpass filter f_n. The DPD filter coefficients, denoted by $\alpha_{p,n}$, are iteratively estimated sample-by-sample or in blocks using the decorrelation-based learning principle (discussed in the next section). The low-power cancellation signal is then obtained by multiplying the filtered-orthogonalized basis functions with their respective DPD filter coefficients $\alpha_{p,n}$. The overall DPD processing is graphically illustrated in Figure 4.3.

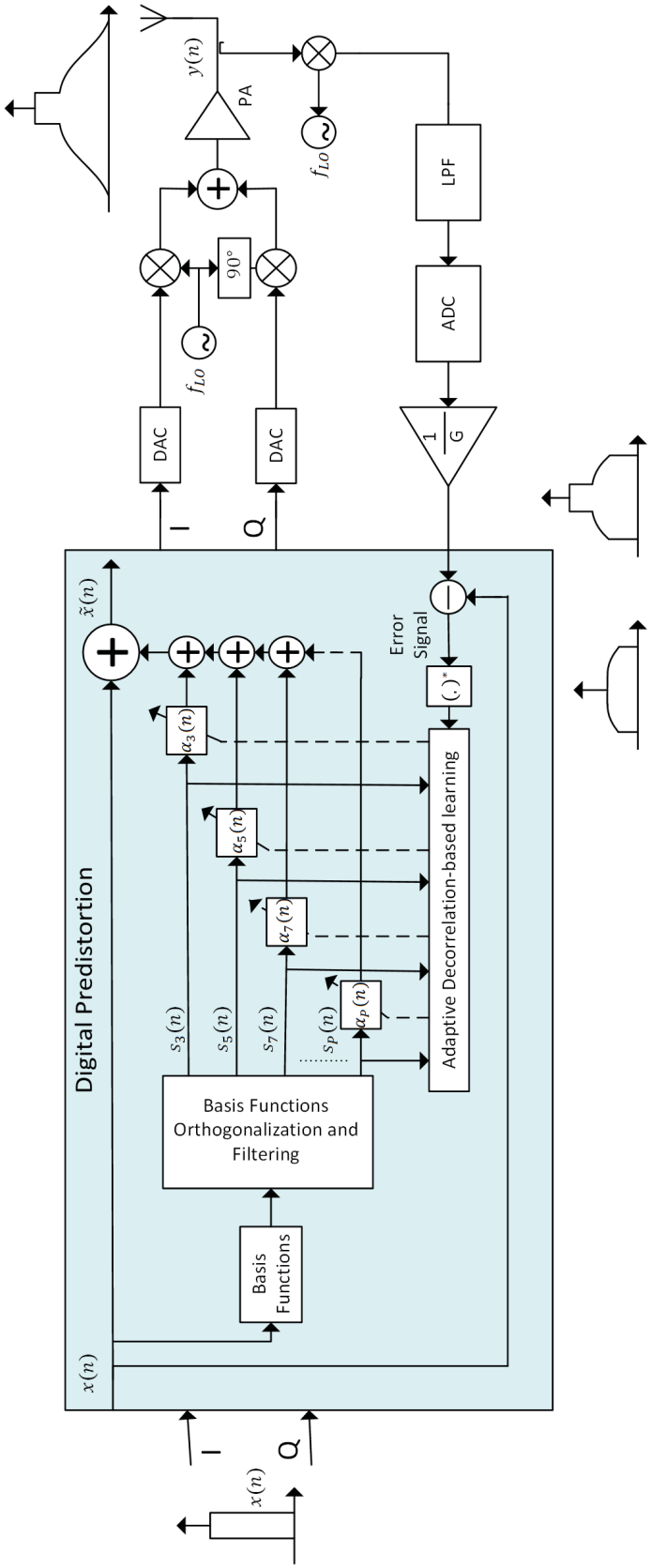

Figure 4.3 *Block diagram of adaptive closed loop sample decorrelation-based Learning.*

The baseband equivalent signal, denoted $\tilde{x}(n)$, from the predistorter into the PA is given by [56]

$$\tilde{x}(n) = x(n) + \sum_{\substack{p=3 \\ p \text{ odd}}}^{P} \alpha_{p,n}^{*} * \mathbf{s}_p(n) \tag{4.15}$$

where $\mathbf{s}_p(n)$ are the basis functions and $\alpha_{p,n}^{*}$ is the complex conjugate of the DPD filter coefficients. The nonlinear distortion suppression achievable is dependent on the selection and optimization of the DPD filter coefficients $\alpha_{p,n}$, and this is discussed in the next section.

4.3 DPD Parameter Learning Algorithm

The closed loop DPD discussed in subsection 3.6.3 is adopted for parameter learning and for adaptation of the slowly varying changes in the PA, like ageing and temperature variations. The decorrelation-based learning principle is formulated and described in [14] and [56] is employed due to its computational efficiency. Decorrelation-based learning involves the continuous minimization of the correlation between the nonlinear distortion signal $e(n)$ in equation (4.14) and the filtered-orthogonalized basis functions, s_3, s_5, s_7, and s_9. As the correlation decreases, the DPD filter coefficients $\alpha_{p,n}$ are adopted continuously until converges is achieved. The analytic reference solution is obtained by setting the correlation between the basis functions and the nonlinear distortion to zero, i.e. $\mathbf{E}[e(n)\mathbf{s}^{*}(n)] = 0$, where $\mathbf{E}[.]$ denotes the statistical expectation operator, and $\mathbf{s}(n)$ is the basis functions vector $[s_3(n)\ s_5(n) \cdots s_p(n)]$ in a memoryless scenario. However, this solution cannot be obtained in practical PA implementations since the PA parameters need to be known prior to the computations and higher-order statistics of the CC(s) need to be computed also [56].

The decorrelation-based learning has been shown to have better linearization performance and lower complexity compared to other closed loop algorithms, such as the inverse and the minimum mean-squared error (MMSE) solutions. In [22], the performance of the decorrelation-based and inverse methods is evaluated for the suppression of third-order intermodulation in non-contiguous spectrally aggregated dual-carriers with the former outperforming the latter in suppressing the unwanted emissions. Furthermore, the inverse methods involve matrix inversion which are known to be computational intensive. The MMSE solution, which involves the minimization of the power of the nonlinear distortion signal $e(n)$, is shown to achieve

better distortion suppression than the inverse solutions. However, when high-order nonlinearity are involved, the computation of the DPD filter coefficients becomes long and tiresome.

The decorrelation-based learning can be implemented in two ways; by sample adaptive learning or by block adaptive learning and is discussed in the following subsections.

4.3.1 Sample-Adaptive Decorrelation Based Learning

In this section, we introduce the actual learning of the DPD filter coefficients $\alpha_{p,n}$ by minimizing the correlation between the nonlinear distortion signal $e(n)$ and the filtered-orthogonalized basis functions $\mathbf{s}(n)$. In the parameter learning, we use a sample by sample learning where the DPD coefficients $\alpha_{p,n}$ are continuously updated as the correlation $\mathbf{E}[e(n)\mathbf{s}^*(n)]$ reduces. We introduce, the following vectors for notational and computational purposes

$$\mathbf{s}_p(n) = [s_p(n)\ s_p(n-1)\cdots s_p(n-M_p)] \tag{4.16}$$

$$\boldsymbol{\alpha}_p(n) = [\alpha_{p,0}(n)\ \alpha_{p,1}(n)\cdots\alpha_{p,M}(n)] \tag{4.17}$$

$$\bar{\boldsymbol{\alpha}}_p(n) = [\boldsymbol{\alpha}_3(n)^T\ \boldsymbol{\alpha}_5(n)^T\cdots\boldsymbol{\alpha}_P(n)^T]^T \tag{4.18}$$

where $\mathbf{s}_p(n)$ represents the p^{th}-order filtered-orthogonalized basis functions samples up to odd order P, with adaptive DPD filter memory depth M. $\bar{\boldsymbol{\alpha}}_p(n)$ denotes the DPD filter coefficients corresponding to the basis functions samples $\mathbf{s}_p(n)$.

The DPD filter coefficients are updated as correlation reduces as follows

$$\bar{\boldsymbol{\alpha}}_p(n+1) = \bar{\boldsymbol{\alpha}}_p(n) - \frac{\mu}{|\mathbf{s}_p(n)|^2}\mathbf{s}_p(n)e^*(n) \tag{4.19}$$

where μ is the learning rate. The learning rate is normalized by a scaling factor $|\mathbf{s}_p(n)|^2$ which makes the learning robust and stable against the input data dynamics, and philosophically similar to the normalized LMS algorithm in [58]. The update process is illustrated in Figure 4.3. The delay compensation is however not explicitly shown, but should be incorporated in the learning loop for exact sample-to-sample mapping of the data input and feedback receiver output signals. The new DPD filter coefficients update the DPD instantaneous input signal $\tilde{x}(n)$ in equation (4.15). The learning can be viewed in the stochastic Newton root search perspective in which the

successive iterations try to find the optimum value of DPD parameters $\bar{\boldsymbol{\alpha}}_p(n)$ which minimize the ensemble correlation in objective function $\boldsymbol{J}(\bar{\boldsymbol{\alpha}}_p(n)) = \boldsymbol{E}[\mathbf{s}_p(n)e^*(n)]$.

4.3.2 Block Adaptive Decorrelation-Based Learning

The block adaptive algorithm is developed to curb the problem arising from the sample-adaptive system when the learning loop delay in the DPD parameter learning phase becomes large and when a PA has long memory depth, especially under hardware processing constraints. Moreover, in this may consequently affect the DPD filter coefficients convergence and linearization performance, especially in the bandlimited DPD solution where feedback observation filter further increases the learning loop delay.

The increased learning loop delay is alleviated by introducing two blocks which are employed in the learning loop and parameter update. Each learning cycle utilizes K number of samples, while new DPD filter coefficients obtained update a block containing L samples, with $K \leq L$. The optimum choice of the block length is when $K = L$, and there is a further reduction in processing delay when $K < L$ [58]. DPD processing in blocks further mitigates the long learning loop delay problem by facilitating stable operation under hardware and software processing constraints.

The DPD filter coefficients processing matrices and vectors are generated for DPD learning and update for block k, and read

$$\alpha_{\mathbf{p}}(k) = [\alpha_{p,0}(k)\ \alpha_{p,1}(k) \dots \alpha_{p,M_p}(k)]^T \tag{4.20}$$

$$\bar{\alpha}(k) = [\alpha_3(k)^T\ \alpha_5(k)^T \dots \alpha_P(k)^T]^T \tag{4.21}$$

$$\mathbf{s}_p(n_k) = [s_p(n_k)\ s_p(n_k-1) \dots s_p(n_k-M_p)]^T \tag{4.22}$$

$$\bar{\mathbf{s}}(n_k) = [\mathbf{s}_3(n_k)^T\ \mathbf{s}_5(n_k)^T \dots \mathbf{s}_P(n_k)^T]^T \tag{4.23}$$

$$\mathbf{S}(k) = [\bar{\mathbf{s}}(n_k)\ \dots\ \bar{\mathbf{s}}(n_k+K-1)] \tag{4.24}$$

$$\mathbf{e}(k) = [e(n_k)\ \dots\ e(n_k+K-1)]^T \tag{4.25}$$

where n_k represents the first sample of processing block k, $\mathbf{S}(k)$ is the filtered-orthogonalized basis functions processing matrix, while $\mathbf{e}(k)$ is the error signal vector in block k. The DPD parameter update equation can be written as

$$\bar{\alpha}(k+1) = \bar{\alpha}(k) - \frac{\mu}{|\mathbf{S}(k)|^2}\mathbf{S}(k)\mathbf{e}^*(k), \tag{4.26}$$

where $\mathbf{e}^*(k)$ denotes the element-wise conjugated error signal vector, and $\bar{\alpha}(k+1)$ are the new DPD filter coefficients which are applied to the next L DPD update block. The processing results in a computationally-efficient linearization of the nonlinearity in the immediate vicinity of the main signal band, which is highly attractive to the mobile device transceivers. Notice that when block size $K = 1$, the case corresponds to the sample adaptive DPD algorithm discussed in the previous subsection.

5. SIMULATION AND MEASUREMENT RESULTS

In this chapter, the performance of the bandlimited DPD solution is evaluated using both MATLAB computer-based simulation and true RF laboratory measurements. In the simulation studies and analysis, PH PA models extracted from a pratical PAs designed for mobile devices and base stations through true RF measurements are employed. The linearization performance of the bandlimited solution is further compared to the conventional DPD methods, where the entire OOB region is linearized. This is done by developing FIR filters f_n with similar stopband, passband, and transition bands but with variable tap lengths. This enables the optimum selection of the number of taps in a filter depending on the suppression of the OOB emissions required for an application.

The inband waveform purity is evaluated using the EVM metric in [1] while the OOB cancellation is quantified using the adjacent leakage ratio ACLR criteria in [59]. Moreover, a simple complexity analysis is done to evaluate the reduction in computational complexity when bandlimited DPD solution is employed rather than the conventional DPD methods.

The chapter is subdivided into two sections: Section 5.1 covers the simulation studies and results, while in Section 5.2, the RF measurement parameters, procedure, and achieved results using practical PAs are reported. A discussion and comparison between the simulation and RF measurements concludes the chapter.

5.1 Matlab Simulations

5.1.1 Simulation Parameters

The Matlab simulations are carried using an LTE-A input signal, which is denoted as $x(n)$ in the previous chapter, composed of one 20 MHz DL OFDM(A) compo-

nent carrier (CC) with 16-QAM data modulation scheme. Both memoryless and memory-based ninth-order PA models ($P = 9$) identified and formulated using the PH behavioral model from RF measurements of practical PAs, with transmit powers of +22 dBm, are used for evaluation and analysis of the performance of the bandlimited DPD solution compared to the conventional DPD method. Prior to the DPD processing, the transmit signal undergoes through crest factor reduction (CFR) by iterative clipping and filtering method in [60]. The memory-based PA model has a memory depth $M = 1$ (2 memory taps per filter). Figure 5.1 shows the normalized baseband equivalent power spectrum density (PSD) diagrams of the LTE-A input signal, the memoryless PA output signal, and the memory-based PA output signal, and illustrates substantial increase the OOB distortion in the adjacent channels after the PA.

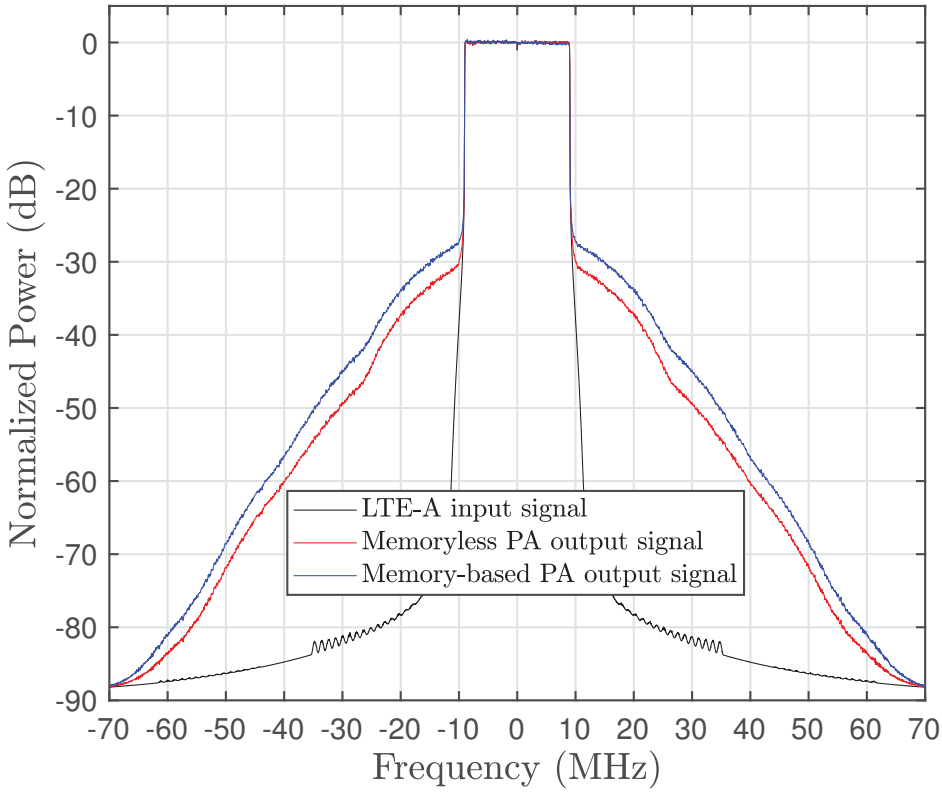

Figure 5.1 *The spectral density of a 20 MHz OFDM carrier and 16-QAM modulation LTE-A signal with transmit power of +22 dBm, before and after a ninth-order memoryless and memory-based PA models.*

In the simulation studies, we design 5 FIR filters with similar stopband, passband,

and transition bands, but with different tap lengths. The filters are developed using the least squares (LS) method in [61] and derived in Appendix A. For computational complexity performance purposes, we arbitrary choose the filters of lengths 11, 21, 31, 41, and 51 taps. These variable filter tap lengths offer a wide platform for evaluating the suppression of unwanted emissions in the OOB region by the bandlimited DPD solution. Furthermore, filter taps longer than 51 would increase computational complexity of the bandlimited DPD and outweigh the benefits accrued from using the filters, i.e, reduction in the DPD sample rates. The FIR filters limit the DPD running bandwidth by filtering the basis functions and feedback observation signals to 3 times the signal bandwidth instead of 9 times (band occupied by the PA output signal and DPD nonlinearity profile). The filters therefore have a passband region up to 30 MHz, 5 MHz transition region, and a stopband starting from 35 MHz on a two-sided frequency spectrum. Figure 5.2 shows the normalized frequency response of the filters.

5.1.2 Simulation Results

The bandlimited DPD solution is evaluated using the block adaptive decorrelation-based learning in both memoryless and memory-based cases using the following parameters: The DPD learning and update block are of the same size, each employing $K = L = 50k$ samples, the number of block estimation iterations are 10, while the DPD memory depth of $M = 1$ (2 memory taps per DPD filter) is employed in the memory-based case. The DPD linearization performance is excellent in both memoryless and memory-based scenarios and is dependent on the number of taps in the filters, as shown in Figure 5.3 and Figure 5.4, and improves with an increase in the number of filter taps.

The performance of the bandlimited decorrelation-based DPD solution is further quantified alongside the conventional DPD method using the widely used metrics, EVM and ACLR criteria. The EVM quantifies the inband waveform purity and is calculated as

$$EVM_{\%} = \sqrt{\frac{P_{error}}{P_{ref}}} \times 100\%, \tag{5.1}$$

where P_{error} and P_{ref} are the power of the error signal and reference signal power of the ideal symbol constellation, respectively. The P_{error} is calculated as difference between the ideal symbol values and the corresponding complex samples at the PA

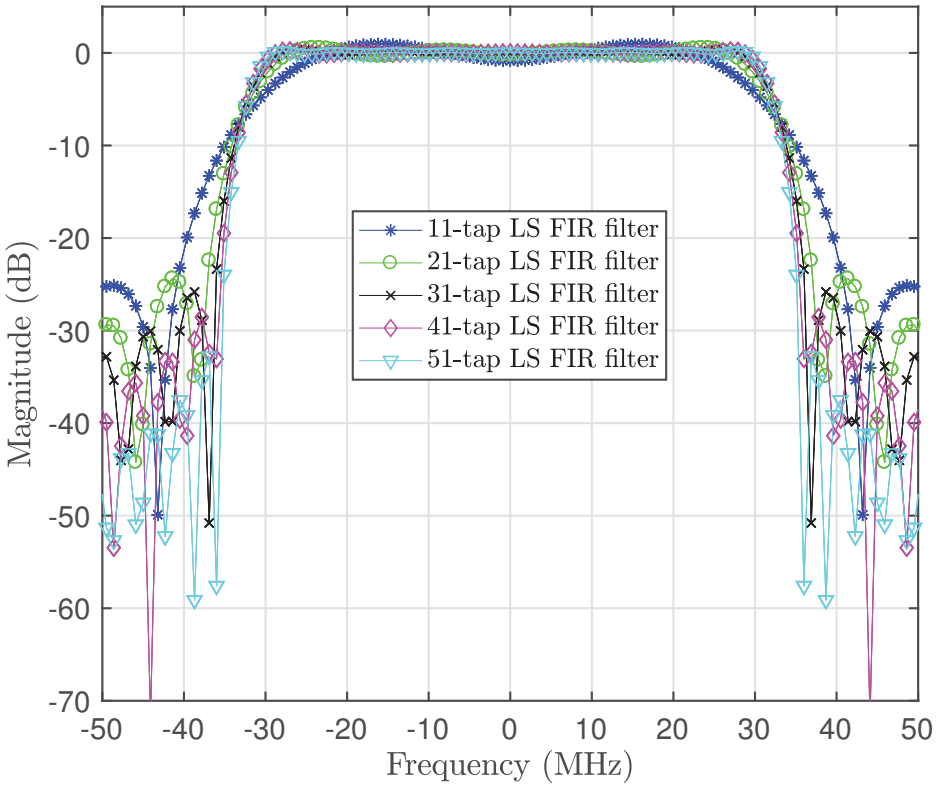

Figure 5.2 *The normalized frequency response of the filter functions used in reducing the DPD running bandwidth. The filter functions have passband region up to 30 MHz, a transition region of 5 MHz, and a stopband starting from 35 MHz.*

output, both synchronized and equalized to have same power, and also normalized to have similar linear gains [62]. While the suppression of the OOB emissions is quantified using the ACLR, which formally defined as the power of the adjacent channel band ($P_{adjacent}$) (in this case, the power of the band linearized by DPD) relative to the power in the main transmit channel (P_{wanted}), written as

$$ACLR_{dB} = 10\log_{10}\frac{P_{wanted}}{P_{adjacent}} \tag{5.2}$$

Table 5.1 and Table 5.2 shows the different ACLR and EVM values of the bandlimited DPD solution compared to the conventional DPD method and unlinearized PA outputs, for both the memoryless and memory-based PA scenarios. The results show excellent suppression of the OOB emissions, with a slight improvement of about 3 -

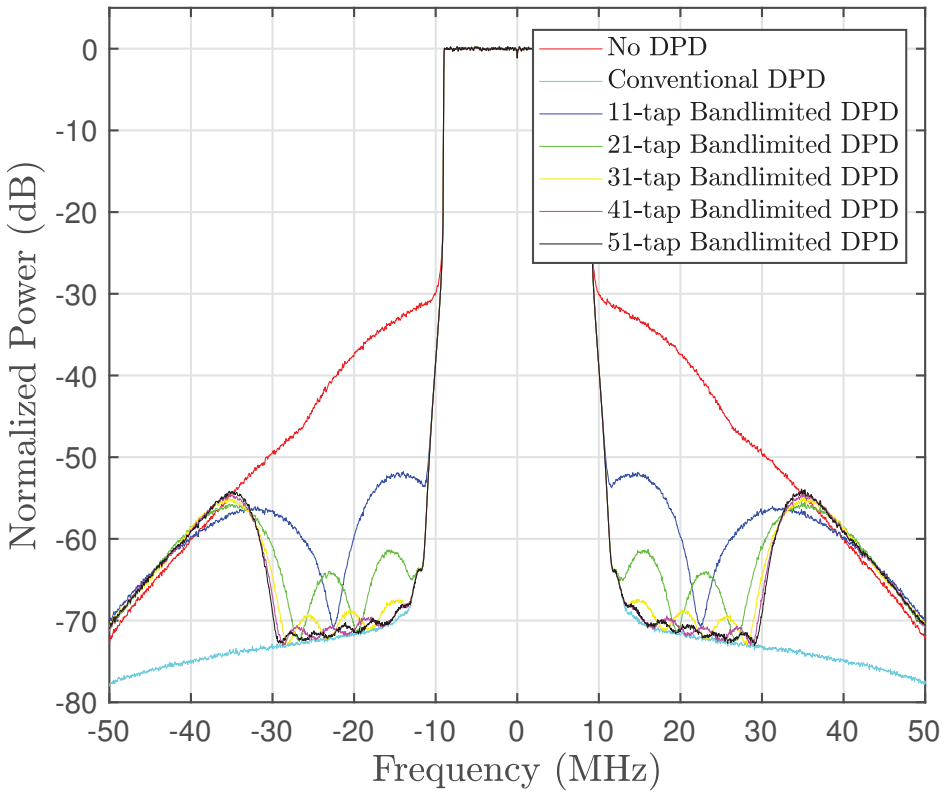

Figure 5.3 *The normalized Power spectral density of the Memoryless PA outputs, with and without DPD, and the bandlimited DPD using variable number of taps.*

4 dB in the ACLR from the 11-tap to 51-tap bandlimited DPD in the memoryless and memory-based PA scenarios. The EVM values are almost similar in both bandlimited cases and conventional DPD, and have remained largely unaffected by the bandlimiting operations during DPD processing.

Figure 5.5 shows smooth and fast convergence of the DPD filter coefficients during the DPD processing due to the basis functions orthogonalization before the bandfiltering stage.

5.2 RF Measurements

In this section, the performance of the bandlimited DPD solution is studied alongside the conventional DPD method in the laboratory setup using practical PAs which are used in RF transmitter chains of mobile devices and base stations. The performance

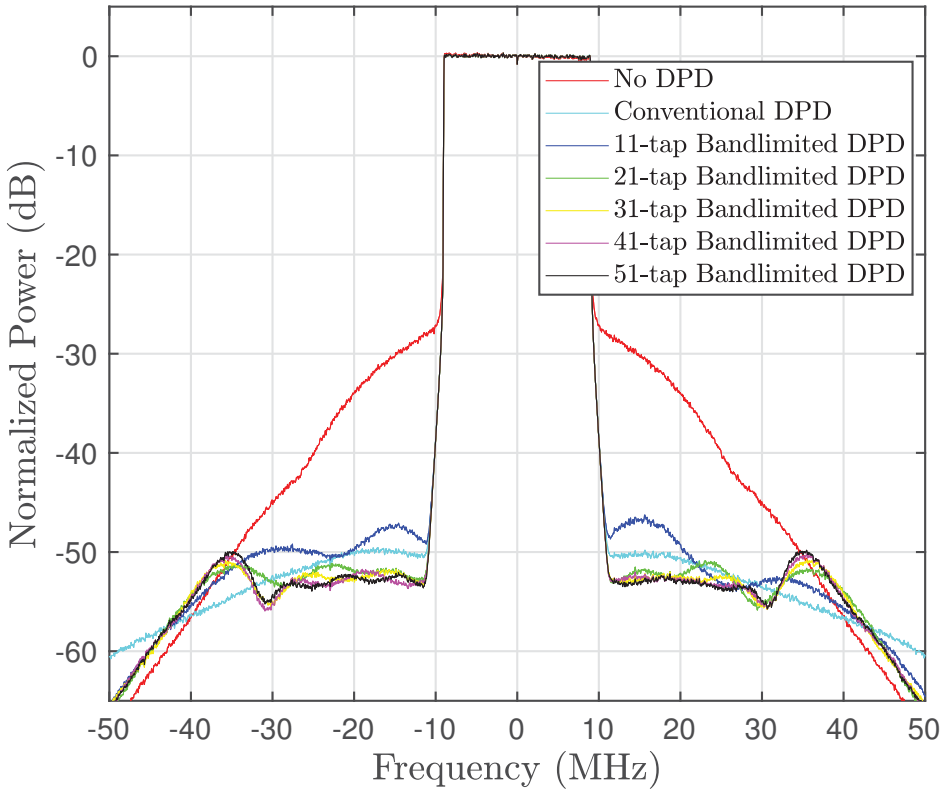

Figure 5.4 *The normalized Power spectral density of the Memory-based PA outputs, with and without DPD, and the bandlimited DPD using variable number of taps.*

of the bandlimited DPD solution in practical PA environment is further quantified using the EVM and ACLR metrics used in the simulation environment to allow for a fair comparison between the two environments. Although the simulation results prove that the bandlimited DPD solution suppresses the PA nonlinearity in the predefined band, it is necessary to confirm and additionally demonstrate using true RF measurements that the bandlimited DPD solution can be used in the actual transmitter environments.

In the subsequent subsections, the measurement setup and the hardware components are discussed in details. The performance of the bandlimited DPD solution is then quantified, and finally we compare the results in the practical PA scenarios with those achieved in the simulation environment.

Table 5.1 *Comparison of the linearization performance of the bandlimited DPD with the Conventional DPD using the EVM and ACLR measures, for the memoryless PA model.*

PAPR = 8.20 dB	**EVM [%]**	**ACLR L/R(dBc)**
No DPD	3.6481	33.224/33.214
With Conventional DPD	0.0275	54.809/54.466
11-tap Bandlimited DPD	0.0579	51.103/50.92
21-tap Bandlimited DPD	0.0635	54.306/53.989
31-tap Bandlimited DPD	0.0735	54.717/54.387
41-tap Bandlimited DPD	0.0999	54.768/54.425
51-tap Bandlimited DPD	0.1076	54.776/54.441

Table 5.2 *Comparison of the linearization performance of the bandlimited DPD with the Conventional DPD using the EVM and ACLR measures, for the memory-based PA model.*

PAPR = 8.18 dB	**EVM [%]**	**ACLR L/R(dBc)**
No DPD	5.4084	33.733/33.788
With Conventional DPD	0.3594	50.939/51.577
11-tap Bandlimited DPD	0.3614	49.822/50.048
21-tap Bandlimited DPD	0.3610	52.234/52.551
31-tap Bandlimited DPD	0.3656	52.511/52.992
41-tap Bandlimited DPD	0.3692	52.595/53.115
51-tap Bandlimited DPD	0.3710	52.707/53.138

5.2.1 Hardware Description and Measurement Setup

The measurement setup used in the RF measurements is shown in Figure 5.6, and is composed of state-of-the-art vector signal transceiver (VST), low-cost power attenuators, and a commercial LTE-A user equipment (UE) and base station (BS) PAs. Two scenarios are evaluated in the RF measurements. First, a UE scenario where the proposed DPD solution performance is evaluated using a LTE-A mobile device PA in an uplink transmission environment. In the second scenario, the bandlimited DPD solution is employed in a downlink BS environment using a commercial high power amplifier (HPA).

The National Instruments (NI) PXIe-5840 VST is employed in our measurements. It combines a vector signal generator (VSG), a vector signal analyzer (VSA), and a high-speed serial data interface. The VST has a frequency range from 9 KHz to 6.5 GHz and a 1 GHz instantaneous bandwidth which are highly desirable in the testing and prototyping of wide bandwidth applications involving carrier aggregation

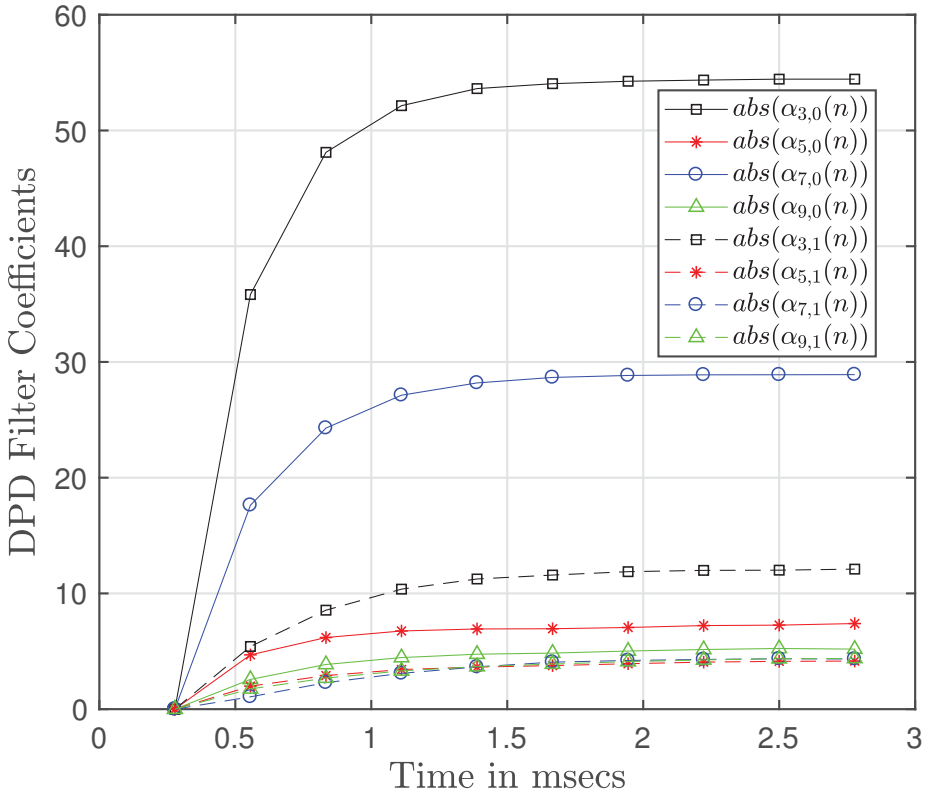

Figure 5.5 *Convergence of the the DPD filter coefficients of the 21-tap bandlimited DPD for the memory-based PA model. It exemplifies fast and steady convergence of the DPD filter coefficients in the bandlimited DPD system.*

scenarios. The VST performs RF I/Q modulation and demodulation while a host processor, embedded through a NI PXIe-8880 controller, runs the bandlimited DPD solution.

An LTE-A input signal composed of one 20 MHz DL OFDM(A) component carrier (CC) with 16-QAM data modulation scheme is also employed in the RF measurement scenarios. Prior to the DPD processing, the transmit signal undergoes through CFR by iterative clipping and filtering. In the conventional DPD method (implemented for reference), the DPD running bandwidth is set to 200 MHz, and the entire nonlinearity profile of the PA is linearized. In the bandlimited case, only the inband and OOB distortions in the immediate vicinity in the carrier are targeted; and consequently the DPD running bandwidth is restrained to 3-times less than conventional bandwidth (i.e. 66.6 MHz) using the 21-tap LS FIR filter. The ban-

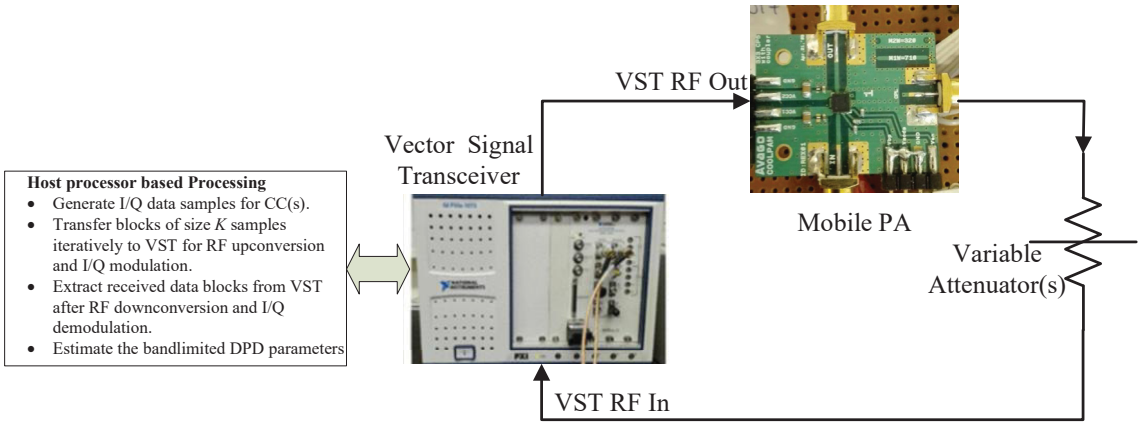

Figure 5.6 *Hardware setup used in the laboratory RF measurement. The setup is used for the UE measurement, while in the BS measurements the mobile PA is replaced by the BS PA and a driver PA.*

dlimited output signal is then down-sampled by a factor of 3 to reduce the DPD sample rate. The above DPD processing parameters are used in both UE and BS measurement scenarios.

5.2.2 UE Measurement Results

The ACPM-5002-TR1 mobile device PA, which has a 29-dB gain and +31-dBm 1-dB compression point, is used for the UE measurements. It is designed for mobile device transmitters for uplink propagation in LTE-A band 25 (1850-1915 MHz). The PA input signal is centred at 1880 MHz for optimum performance of the PA.

The block adaptive decorrelation-based parameter learning is used for the evaluation and quantification of the bandlimited DPD solution. The host processor generates the digital baseband input signal, which is then subdivided into 8 parameter learning blocks of size K = $50k$ samples each. The blocks are then transferred iteratively to the VSG for RF upconversion and I/Q modulation to the PA transmit frequency range and at desired input power level. The VSG output signal is then relayed to the PA input port via the VST RF output port. The PA feedback observation signal is coupled back to the VST RF input port through two attenuators, the 8493A coaxial fixed attenuator and the SMA fixed attenuator, whose resultant attenuation is 40 dB.

The VSA then performs RF downconversion and I/Q demodulation to bring the

signal back to baseband, where the band-filtering and the nonlinear distortion calculation also takes place. The linear gain of the entire RF and feedback chain is extracted using the block LS before the nonlinear signal extraction. In the DPD filter coefficients learning, the DPD nonlinearity order $P = 9$ and the memory depth $M = 3$ (four taps per basis function) is adopted for both the bandlimited and conventional DPD solutions.

The bandlimited DPD solution outperforms the conventional DPD method in the suppression of the OOB distortions in the immediate vicinity as shown in Figure 5.7 and Table 5.3. The ACLR values in the bandlimited DPD solution are better than conventional DPD method while the EVM in both cases are largely similar.

Table 5.3 *Comparison of the linearization performance of the bandlimited DPD with the Conventional DPD using the EVM and ACLR measures, for the LTE-A mobile device PA.*

PAPR = 7.2 dB	**EVM [%]**	**ACLR L/R(dBc)**
No DPD	3.3300	36.0209/38.6568
With Conventional DPD	1.1967	46.2729/48.2580
21-tap Bandlimited DPD	1.0536	48.5089/48.5686

5.2.3 Base Station Measurement Results

A commercial base station PA, designed for LTE-A downlink (DL) Band 3 (1805 - 1880 MHz) is used in the RF measurements. It has a gain of 42 dB and its maximum output power is 49.4 dBm. A driver PA (model no. ZFL-2500 VH), with 25-dB gain, is employed before the main PA to boost its input power level. Like in the UE measurements, the block adaptive decorrelation-based algorithm is adopted for DPD filter coefficients learning. The baseband equivalent input signal, generated by the host processor, is subdivided into 16 parameter learning block of size $K = 15k$ samples each. The DPD stage output signal blocks are then transferred iteratively to the VSG for RF up-conversion and I/Q modulation before being injected to the main PA via the driver PA, as shown in Figure 5.6. The PA output observation signal is extracted from the PA's feedback port, which has 40-dB coupling factor from main PA output, and then fed to the VST RF output port via a 30-dB attenuator.

The basis functions and the feedback observation signal blocks, are then filtered using the 21-tap LS FIR filter before being decimated at the lower sample rate to

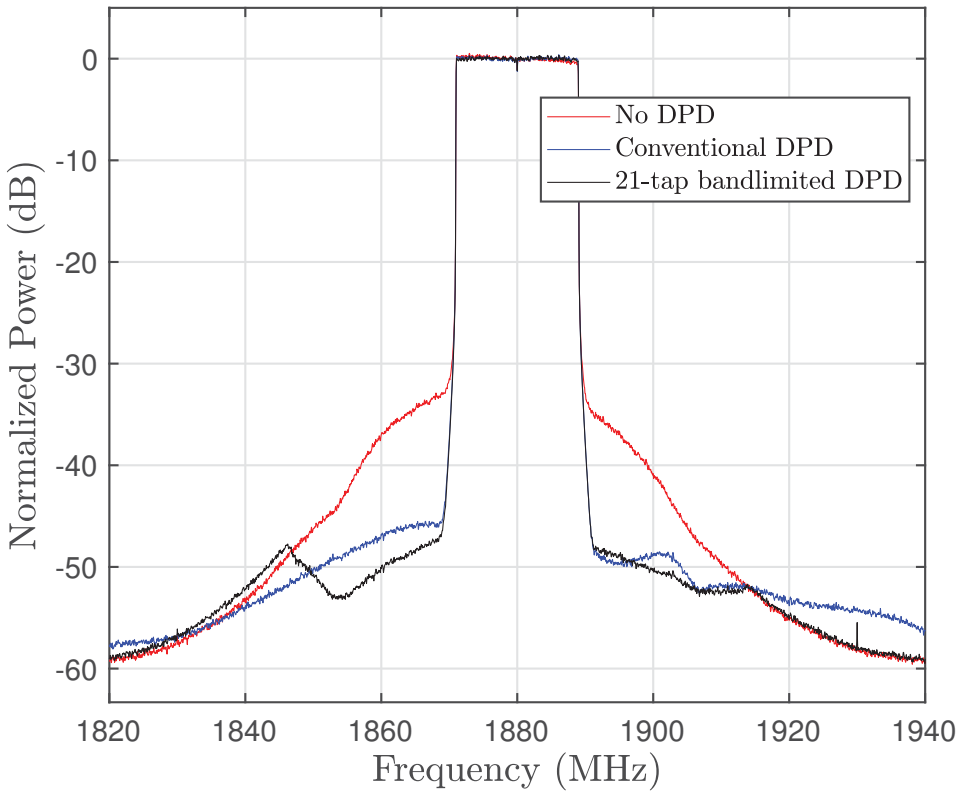

Figure 5.7 *The normalized PA output power spectral density of the conventional DPD compared to the 21-tap bandlimited DPD for a UE LTE-A PA for a single 20 MHz component carrier operating at an output power of +21 dBm.*

reduce the DPD running bandwidth and complexity. The DPD filter coefficients are then computed using the block adaptive decorrelation-based principle and used to filter the next block of parameters. Like in the UE measurements, the DPD nonlinearity order $P = 9$ and the memory depth $M = 3$ (four taps per basis function) are adopted for both the bandlimited and conventional DPD solutions.

Figure 5.8 and Table 5.4 shows the normalized PSDs of the bandlimited DPD solution compared to the conventional DPD method and the corresponding EVM and ACLR results, respectively. The results further confirm better performance of the bandlimited DPD in the ACLR measurement region, despite using fewer samples in the DPD learning blocks to reduce computational complexity.

Table 5.4 *Comparison of the linearization performance of the bandlimited DPD with the Conventional DPD using the EVM and ACLR measures for a Commercial Base Station PA.*

PAPR = 7.18 dB	**EVM [%]**	**ACLR L/R(dBc)**
No DPD	3.0812	34.9156/38.5417
With Conventional DPD	1.1472	48.5828/47.9941
21-tap Bandlimited DPD	1.0762	50.7091/48.7817

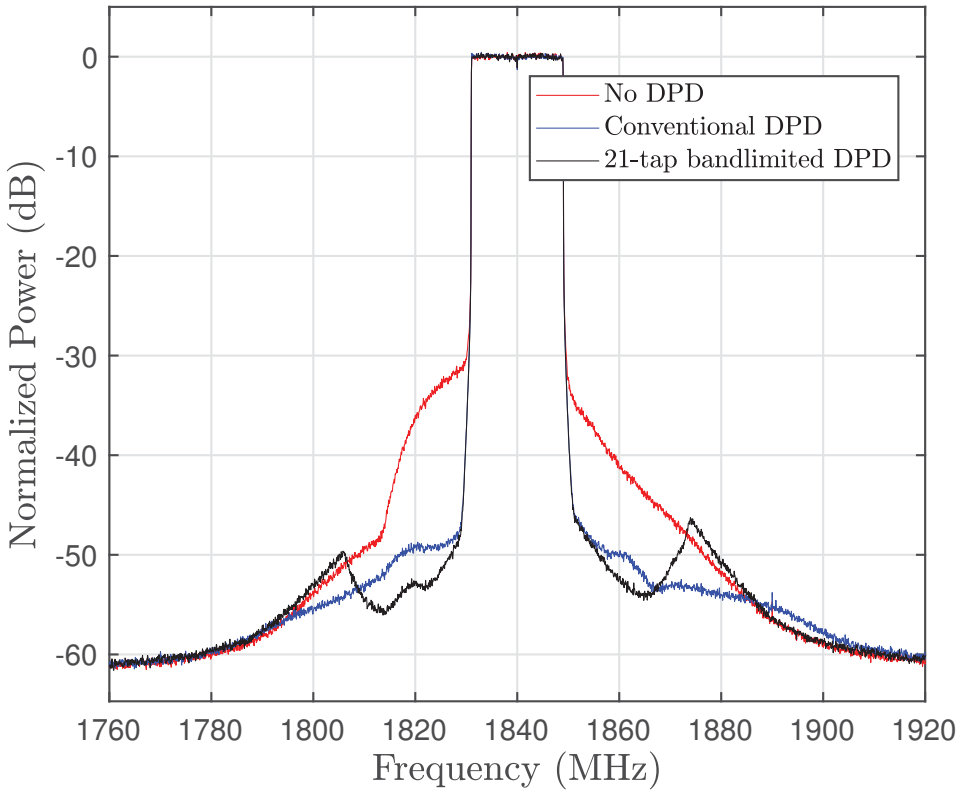

Figure 5.8 *The normalized PA output power spectral density of the conventional DPD compared to the 21-tap bandlimited DPD for a BS HPA for a single 20 MHz component carrier operating at an output power of +49.4 dBm.*

5.3 Discussion

This chapter has presented the results of the bandlimited DPD concept proposed in Chapter 4. The bandlimited DPD has been evaluated using computer simulations and practical RF measurements to ascertain the viability and usability in

the real transmitter chain environments. The proposed DPD solution performance is compared to the conventional DPD method in two computer simulation scenarios using memoryless and memory-based PH PA models as well as commercial UE and BS PAs. The DPD running bandwidth is reduced by filtering the PA feedback observation signal and basis functions using FIR filters thereby reducing the band linearized using DPD. To reduce computational complexity, the sample rates of the bandlimited DPD solution are reduced by decimating the signals prior to the decorrelation-based learning. In all the above scenarios, there is a reduction in the minimum required DPD sample rates. For instance, in the simulation studies, the sample rates are reduced from 180 MSPS to 100 MSPS, which consequently leads to a significant reduction in the number of FLOPs per second (FLOPs) required for the generation of basis functions and DPD coefficients filtering.

The memoryless PA model results show a consistent tread in the improvement of ACLR of the bandlimited DPD solution as the number of filter taps, which is rather obvious. However, as the filter taps increase, there is no significant increase in the ACLR and the value tends to approach the conventional DPD's value. In the memory-based PA model and practical PAs RF measurements, the bandlimited DPD solution outperforms the conventional DPD method when filter taps are equal or more than 21. This is attributed to the application of the DPD filter coefficients on a narrower frequency band thereby outperforming the conventional DPD method in the suppression of the spectral regrowth in the ACLR measurement region. In all the bandlimited DPD solution scenarios, the EVM values remain largely similar with the corresponding conventional DPD values, implying a good performance in the restoration of the inband waveform purity.

The results are consistent in the memory-based PA model and the commercial PAs, which is an interesting finding, in that the bandlimited DPD solution offers an extra 1 - 2 dB spectral regrowth suppression. The bandlimited decorrelation-based learning may become inevitable when extra distortion cancellation is required to suppress a persistent part of the spectral regrowth because of the sample rates reduction and improved ACLR performance. Furthermore, the solution offers a computationally-efficient process which is attractive for the battery powered devices and small BSs. However, for the benefits of the bandlimited DPD solution to be fully leveraged, the extra computations introduced by the filter functions f_n should be less than the reduction in computations obtained from using lower DPD sample rates. In this way, the power consumption of the entire RF transmission chain is reduced while

achieving better unwanted emission suppression.

6. CONCLUSION

In this thesis, a bandlimited DPD solution is studied for mitigation of nonlinear distortion in wideband spectrum access involving a single carrier or contiguous CA of two or more CCs. The reduced-complexity decorrelation-based principle formulated in [14] for suppression of unwanted emissions is applied in the studied bandlimited DPD concept. The performance of the bandlimited DPD solution is compared to the conventional DPD method using the well-known ACLR and EVM metrics.

The studied bandlimited DPD solution involves the use of DPD for the suppression of the inband distortion and spectrum regrowth in the immediate vicinity, while unwanted emissions more far away in the spectrum from the main carrier(s) are suppressed using transmit filters or ignored if they don't violate the emission limits. The use of wide bandwidths of up to 100 MHz proposed in future LTE-A implementations may make classical DPD methods infeasible due to the high speed requirements for the DACs, transmitter, and receiver chains. Recent works in literature have concentrated in the development of the bandlimited DPD methods using the ILA, which is more computationally-complex compared to the decorrelation based principle.

The bandlimited DPD solution studied aims at reducing the DPD running bandwidth using FIR filters to limit the bandwidth expansion during basis functions generation and to filter the bandwidth of the feedback observation signal from the PA output. The resultant signal blocks are then decimated to reduce the sample rates, before the DPD filter coefficients are computed using the decorrelation-based learning, as explained in Chapter 4. The DPD processing stage therefore becomes computationally-efficient due to reduction in the number of computations performed on the parameters to obtain the DPD filter coefficients. Furthermore, the PH PA model used in the generation of the basis functions requires less running complexity than Volterra series and is shown to accurately model nonlinear distortions in practical PAs [17].

To ascertain the viability of the bandlimited DPD solution, Matlab-based simulations using PH PA models extracted from practical PAs as well as true RF measurements using commercial PAs used in RF front-ends were performed. The first scenario involved the use of a memoryless PH PA model in which the bandlimited DPD solution is outperformed by the conventional DPD method in both the suppression of the inband distortions and OOB emissions in all the cases. However, there is an improvement in the ACLR performance as the number of filter taps increase. The other matlab-based simulation scenario involves the use of the memory-based PH PA model, while the RF measurements utilize two commercial PAs used in UE and BS transmitter chains. In all the scenarios, the bandlimited DPD solution performs better than the conventional DPD method in the suppression of spectral regrowth within the ACLR measurement regions when an FIR filter with 21 or more taps is used. The achieved inband waveform purity is largely similar for all the test runs. Overall, the ACLR values are approximately 1-2 dB higher than those of the conventional DPD method.

The bandlimited DPD solution explored offers better linearization performance under hardware and software constraints due to its low-complexity decorrelation-based learning principle. Furthermore, the solution alleviates the DPD bandwidth constraints associated with wideband LTE-A implementations by offering designers flexibility to choose the bandwidth to be linearized. The practical applicability of the bandlimited DPD solution is therefore enhanced, as the linearization performance is improved while reducing the complexity of the DPD.

BIBLIOGRAPHY

[1] *LTE Evolved Universal Terrestrial Radio Access (E-UTRA): User Equipment (UE) Radio Transmission and Reception*, document 3GPP TS 36.101 V13.3.0 (Release 13), May 2016.

[2] J. Proakis and M. Salehi, *Digital Communications*. McGraw-Hill, 2008. [Online]. Available: https://books.google.fi/books?id=IllBngAACAAJ

[3] G. Fettweis, M. Lohning, D. Petrovic, M. Windisch, P. Zillmann, and W. Rave, "Dirty rf: a new paradigm," in *2005 IEEE 16th International Symposium on Personal, Indoor and Mobile Radio Communications*, vol. 4, Sept 2005, pp. 2347–2355 Vol. 4.

[4] A. M. Wyglinski, "Physical layer loading algorithms for indoor wireless multicarrier systems," Ph.D. dissertation, McGill University, 2004.

[5] S. Cripps, *RF Power Amplifiers for Wireless Communications*, ser. Artech House microwave library.

[6] *Unwanted Emissions in the Spurious Domain*, document Rec. ITU-R SM.329-12, Int. Telecommun. Union Radio Commun. Sector, Sep. 2012.

[7] A. Kiayani, M. Abdelaziz, L. Anttila, V. Lehtinen, and M. Valkama, "Digital mitigation of transmitter-induced receiver desensitization in carrier aggregation fdd transceivers," *IEEE Transactions on Microwave Theory and Techniques*, vol. 63, no. 11, pp. 3608–3623, Nov 2015.

[8] M. Abdelaziz, L. Anttila, and M. Valkama, "Digital predistortion for mitigating transmitter-induced receiver desensitization in carrier aggregation fdd transceivers," in *2016 IEEE Global Conference on Signal and Information Processing (GlobalSIP)*, Dec 2016, pp. 694–698.

[9] A. Katz, "Linearization: reducing distortion in power amplifiers," in *IEEE Microwave Magazine*, vol. 2, no. 4, pp. 37-49, Dec 2001.

[10] A. Mohammadi and F. M. Ghannouchi, *RF Power Amplifier and Linearization Techniques*. Berlin, Heidelberg: Springer Berlin Heidelberg, 2012, pp. 77–128.

[11] J. K. Cavers, "Amplifier linearization using a digital predistorter with fast adaptation and low memory requirements," *IEEE Transactions on Vehicular Technology*, vol. 39, no. 4, pp. 374–382, Nov 1990.

[12] W.-J. Kim, S. P. Stapleton, J. H. Kim, and C. Edelman, "Digital predistortion linearizes wireless power amplifiers," *IEEE Microwave Magazine*, vol. 6, no. 3, pp. 54–61, Sept 2005.

[13] F. Luo, *Digital Front-End in Wireless Communications and Broadcasting: Circuits and Signal Processing*. Cambridge University Press, 2011. [Online]. Available: https://books.google.fi/books?id=Tu_c9XmSD1UC

[14] M. Abdelaziz, L. Anttila, C. Tarver, K. Li, J. R. Cavallaro, and M. Valkama, "Low-complexity subband digital predistortion for spurious emission suppression in noncontiguous spectrum access," *IEEE Transactions on Microwave Theory and Techniques*, vol. 64, no. 11, pp. 3501–3517, Nov 2016.

[15] Z. Fu, L. Anttila, M. Abdelaziz, M. Valkama, and A. M. Wyglinski, "Frequency-selective digital predistortion for unwanted emission reduction," *IEEE Transactions on Communications*, vol. 63, no. 1, pp. 254–267, Jan 2015.

[16] M. Abdelaziz, A. Ghazi, L. Anttila, J. Boutellier, T. Lähteensuo, X. Lu, J. R. Cavallaro, S. S. Bhattacharyya, M. Juntti, and M. Valkama, "Mobile transmitter digital predistortion: Feasibility analysis, algorithms and design exploration," in *2013 Asilomar Conference on Signals, Systems and Computers*, Nov 2013, pp. 2046–2053.

[17] A. S. Tehrani, H. Cao, S. Afsardoost, T. Eriksson, M. Isaksson, and C. Fager, "A comparative analysis of the complexity/accuracy tradeoff in power amplifier behavioral models," *IEEE Transactions on Microwave Theory and Techniques*, vol. 58, no. 6, pp. 1510–1520, June 2010.

[18] J. C. Pedro and S. A. Maas, "A comparative overview of microwave and wireless power-amplifier behavioral modeling approaches," *IEEE Transactions on Microwave Theory and Techniques*, vol. 53, no. 4, pp. 1150–1163, April 2005.

[19] M. Isaksson, D. Wisell, and D. Ronnow, "A comparative analysis of behavioral models for rf power amplifiers," *IEEE Transactions on Microwave Theory and Techniques*, vol. 54, no. 1, pp. 348–359, Jan 2006.

[20] C. Yu, L. Guan, and A. Zhu, "Band-limited volterra series-based behavioral modeling of rf power amplifiers," in *2012 IEEE/MTT-S International Microwave Symposium Digest*, June 2012, pp. 1–3.

[21] C. Yu, L. Guan, E. Zhu, and A. Zhu, "Band-limited volterra series-based digital predistortion for wideband rf power amplifiers," *IEEE Transactions on Microwave Theory and Techniques*, vol. 60, no. 12, pp. 4198–4208, Dec 2012.

[22] M. Abdelaziz, L. Anttila, A. Mohammadi, F. Ghannouchi, and M. Valkama, "Reduced-complexity power amplifier linearization for carrier aggregation mobile transceivers," in *2014 IEEE International Conference on Acoustics, Speech and Signal Processing (ICASSP)*, May 2014, pp. 3908–3912.

[23] M. Abdelaziz, L. Anttila, A. Kiayani, and M. Valkama, "Decorrelation-based concurrent digital predistortion with a single feedback path," *IEEE Transactions on Microwave Theory and Techniques*, vol. PP, no. 99, pp. 1–14, 2017.

[24] F. M. Ghannouchi and O. Hammi, "Behavioral modeling and predistortion," *IEEE Microwave Magazine*, vol. 10, no. 7, pp. 52–64, Dec 2009.

[25] J. H. K. Vuolevi and T. Rahkonen, "Extraction of a nonlinear ac fet model using small-signal s-parameters," *IEEE Transactions on Microwave Theory and Techniques*, vol. 50, no. 5, pp. 1311–1315, May 2002.

[26] P. Asbeck, "Linearisation of rf power amplifiers," Ph.D. dissertation, Technical University of Denmark, 2001.

[27] R. Raich and G. T. Zhou, "On the modeling of memory nonlinear effects of power amplifiers for communication applications," in *Proceedings of 2002 IEEE 10th Digital Signal Processing Workshop, 2002 and the 2nd Signal Processing Education Workshop.*, Oct 2002, pp. 7–10.

[28] R. Raich, "Nonlinear system identification and analysis with applications to power amplifier modeling and power amplifier predistortion," Ph.D. dissertation, Georgia Institute of Technology, 2004.

[29] A. E. Nordsjo, "An algorithm for adaptive predistortion of certain time-varying nonlinear high-power amplifiers," in *RADAR 2002*, Oct 2002, pp. 469–473.

[30] J. Voros, "Modeling and identification of wiener systems with two-segment nonlinearities," *IEEE Transactions on Control Systems Technology*, vol. 11, no. 2, pp. 253–257, Mar 2003.

[31] A. A. M. Saleh, "Frequency-independent and frequency-dependent nonlinear models of twt amplifiers," *IEEE Transactions on Communications*, vol. 29, no. 11, pp. 1715–1720, November 1981.

[32] E. Costa, M. Midrio, and S. Pupolin, "Impact of amplifier nonlinearities on ofdm transmission system performance," *IEEE Communications Letters*, vol. 3, no. 2, pp. 37–39, February 1999.

[33] Y. Guo and J. R. Cavallaro, "A novel adaptive pre-distorter using ls estimation of sspa non-linearity in mobile ofdm systems," in *2002 IEEE International Symposium on Circuits and Systems. Proceedings (Cat. No.02CH37353)*, vol. 3, 2002, pp. III–453–III–456 vol.3.

[34] A. Ghorbani and M. Sheikhan, "The effect of solid state power amplifiers (sspas) nonlinearities on mpsk and m-qam signal transmission," in *1991 Sixth International Conference on Digital Processing of Signals in Communications*, Sep 1991, pp. 193–197.

[35] C. Rapp, "Effects of HPA-nonlinearity on a 4DPSK/OFDMsignal for a digital sound broadcasting system, "in Proceedings of the Second European Conference on Satellite Communications, pp. 179- 184,Liege, Belgium, Oct. 22-24, 1991.

[36] G. P. White, A. G. Burr, and T. Javornik, "Modelling of nonlinear distortion in broadband fixed wireless access systems," *Electronics Letters*, vol. 39, no. 8, pp. 686–687, April 2003.

[37] S. Boumaiza and F. M. Ghannouchi, "Thermal memory effects modeling and compensation in rf power amplifiers and predistortion linearizers," *IEEE Transactions on Microwave Theory and Techniques*, vol. 51, no. 12, pp. 2427–2433, Dec 2003.

[38] J.Mathews and G. Sicuranza, *Polynomial Signal Processing.* New York, USA: John Wiley Sons, 2000.

[39] M. Schetzen, The Volterra and Wiener Theories of Nonlinear Systems, reprint ed. Melbourne, FL: Krieger, 1989.

[40] A. Zhu, J. C. Pedro, and T. J. Brazil, "Dynamic deviation reduction-based volterra behavioral modeling of rf power amplifiers," *IEEE Transactions on Microwave Theory and Techniques*, vol. 54, no. 12, pp. 4323–4332, Dec 2006.

[41] J. Kim and K. Konstantinou, "Digital predistortion of wideband signals based on power amplifier model with memory," *Electronics Letters*, vol. 37, no. 23, pp. 1417–1418, Nov 2001.

[42] D. R. Morgan, Z. Ma, J. Kim, M. G. Zierdt, and J. Pastalan, "A generalized memory polynomial model for digital predistortion of rf power amplifiers," *IEEE Transactions on Signal Processing*, vol. 54, no. 10, pp. 3852–3860, Oct 2006.

[43] F. M. Ghannouchi, O. Hammi, and M. Helaoui, *Behavioral Modelling and Predistortion of Wideband Wireless Transmitters*, 1st ed. GB: John Wiley Sons Inc, 2015.

[44] J. Armstrong, "Peak-to-average power reduction for ofdm by repeated clipping and frequency domain filtering," *Electronics Letters*, vol. 38, no. 5, pp. 246–247, Feb 2002.

[45] Jiang, T. and Wu, Y. (2008) An overview: peak-to-average power ratio reduction techniques for OFDM signals. IEEE Transactions on Broadcasting , 54 (2), 257– 268.

[46] Han, S.H. and Lee, J.H. (2005) An overview of peak-to-average power ratio reduction techniques for multi-carrier transmission. IEEE Wireless Communications , 12 (2), 56– 65.

[47] P. Kenington, *High-linearity RF Amplifier Design*, ser. Artech House microwave library. Artech House, 2000. [Online]. Available: https://books.google.fi/books?id=qQhTAAAAMAAJ

[48] H. Kosugi, T. Matsumoto, T. Uwano, "A High-Efficiency Linear Power Amplifier Using an Envelope Feedback Method", Electronics and Communications in Japan, Part 2, Vol. 77, No. 3, 1994.

[49] P. E. Kenington, High-linearity RF Amplifier Design , Artech House, 2000.

[50] D. Cox, "Linear amplification with nonlinear components," *IEEE Transactions on Communications*, vol. 22, no. 12, pp. 1942–1945, Dec 1974.

[51] B. Stengel and W. R. Eisenstadt, "Linc power amplifier combiner method efficiency optimization," *IEEE Transactions on Vehicular Technology*, vol. 49, no. 1, pp. 229–234, Jan 2000.

[52] A. Bateman, "The combined analogue locked loop universal modulator (callum)," in *[1992 Proceedings] Vehicular Technology Society 42nd VTS Conference - Frontiers of Technology*, May 1992, pp. 759–763 vol.2.

[53] J. Wood, *Behavioral Modeling and Linearization of RF Power Amplifiers*. Norwood: Artech House Inc, 2014.

[54] H. Paaso and A. Mammela, "Comparison of direct learning and indirect learning predistortion architectures," in *2008 IEEE International Symposium on Wireless Communication Systems*, Oct 2008, pp. 309–313.

[55] R. N. Braithwaite, "A comparison of indirect learning and closed loop estimators used in digital predistortion of power amplifiers," in *2015 IEEE MTT-S International Microwave Symposium*, May 2015, pp. 1–4.

[56] M. Abdelaziz, L. Anttila, and M. Valkama, "Reduced-complexity digital predistortion for massive mimo," in *2017 IEEE International Conference on Acoustics, Speech and Signal Processing (ICASSP)*, March 2017, pp. 6478–6482.

[57] H. Qian, S. Yao, H. Huang, and W. Feng, "A low-complexity digital predistortion algorithm for power amplifier linearization," *IEEE Transactions on Broadcasting*, vol. 60, no. 4, pp. 670–678, Dec 2014.

[58] S. Haykin and S. Haykin, *Adaptive Filter Theory*. Pearson, 2014. [Online]. Available: https://books.google.fi/books?id=J4GRKQEACAAJ

[59] 3GPP Evolved Universal Terrestrial Radio Access (E-UTRA); User Equipment (UE) radio transmission and reception, 3rd Generation Partnership Project (3GPP), Cedex, France. [Online]. Available: http://www.3gpp.org/ftp/Specs/html-info/36101.htm.

[60] J. Armstrong, "Peak-to-average power reduction for ofdm by repeated clipping and frequency domain filtering," *Electronics Letters*, vol. 38, no. 5, pp. 246–247, Feb 2002.

[61] T. W. Parks and C. S. Burrus, Digital Filter Design, New York: John Wiley and Sons, Inc., June 1987, contains FORTRAN software listings.

[62] E. Dahlman, S. Parkvall, and J. Skold, 4G LTE/LTE-Advanced for Mobile Broadband. Amsterdam, The Netherlands: Elsevier, 2011.

APPENDIX A

Here, we derive the LS solution for the optimization of the FIR filters designed to reduce the DPD running bandwidth. The FIR filters are of length L taps/coefficients, with L odd. The filters are centered at the origin and with linear phase. The frequency response $H(w_k)$ of the filters is given by,

$$H(w_k) = \sum_{n=-(L-1)/2}^{(L-1)/2} b_n e^{-jw_k n} \tag{6.1}$$

where b_n are the coefficients of the filters. The filters have even symmetry around the time axis, the coefficients can be shifted to the right to make them causal while still maintaining a linear phase. The frequency response is therefore a real signal, which can be written as,

$$H(w_k) = b_0 + 2 \sum_{n=1}^{(L-1)/2} b_n \cos(w_k n), \quad k = 0, 1, 2, \cdots, N-1. \tag{6.2}$$

The equation can alternatively be written in matrix form as,

$$\underbrace{\begin{bmatrix} 1 & 2\cos(w_0) & \dots & 2\cos[w_0((L-1)/2)] \\ 1 & 2\cos(w_1) & \dots & 2\cos[w_1((L-1)/2)] \\ \vdots & \vdots & \ddots & \vdots \\ 1 & 2\cos(wN_1) & \dots & 2\cos[w_{N-1}((L-1)/2)] \end{bmatrix}}_{A} \underbrace{\begin{bmatrix} b_0 \\ b_1 \\ \vdots \\ b_{(L-1)/2} \end{bmatrix}}_{\mathbf{b}} = \underbrace{\begin{bmatrix} H(w_0) \\ H(w_1) \\ \vdots \\ H(w_{N-1}) \end{bmatrix}}_{\mathbf{d}} \tag{6.3}$$

where $\mathbf{d}$ is the vector of the desired frequency response with the minimum error magnitude obtained by optimizing the maximum frequency response A over the frequency axis with the coefficients $\mathbf{b}$. We minimize the error by computing the coefficients using the LS algorithm

$$\mathbf{b}_{LS} = \arg \min_{\mathbf{b}} ||A\mathbf{b} - \mathbf{d}||^2. \tag{6.4}$$

From this, we obtain the normal equation,

$$A^T A\mathbf{b} = A^T \mathbf{d} \tag{6.5}$$

and finally, the optimum value of the coefficients $\mathbf{b}$ is given by

$$\mathbf{b} = [(A^T A)^{-1} A^T]\mathbf{d}. \tag{6.6}$$